Acta Geochim (2025) 44:700–730
https://doi.org/10.1007/s11631-024-00749-4

ORIGINAL ARTICLE

Petrogenesis of the Jaisamand sanukitoids and associated TTGs: Constraints on the Neoarchean tectonic evolution of the southern Aravalli-Banded Gneissic Complex, northwest India

Prabhakar Dutta[1] · Parampreet Kaur[1] · Naveen Chaudhri[1] · Swati Sharma[1]

Received: 17 September 2024 / Revised: 18 October 2024 / Accepted: 20 November 2024 / Published online: 26 December 2024

Abstract The lack of a comprehensive whole-rock geochemical and mineralogical dataset for the Archean granitoids of the Aravalli-Banded Gneissic Complex (BGC), northwest India, results in significant challenges for their correct characterization and assessment of their antiquity. The new field, mineralogical and geochemical data classify the Jaisamand granitoids into sanukitoids, TTGs, and transitional TTGs, which are most likely coeval in nature. The obtained results, in conjuncture with the previously published geochemical and geochronological results of the Aravalli–BGC granitoids, unveil the Neoarchean affinity of the Jaisamand pluton. The TTGs were generated by the melting of a subducting slab (metabasite) at shallow (high-HREE-Y TTGs) to moderate depths (medium-HREE-Y TTGs) above the garnet-in line but still within the plagioclase stability field, with garnet-poor residue. The ascending TTG melts were transformed into sanukitoids through differential interaction with the overlying mantle wedge peridotite. The TTG melts, generated at different pressures, interacted with older TTGs at lower and middle crustal levels to form the transitional TTGs. The coexistence of high-HREE-Y and medium-HREE-Y TTGs and sanukitoids suggests a subduction-related setting for the Jaisamand granitoids. The heat required for simultaneous melting at shallow and deeper depths during the Neoarchean was provided by the upwelling asthenosphere due to slab break-off. The study also revealed the occurrence of altered granitoids in the Jaisamand pluton, showing evidence of albitization and silicification. These rocks do not represent the pristine mineralogy and should be carefully examined to avoid misleading interpretations, particularly for the Archean granitoids.

Keywords Aravalli-Banded Gneissic Complex · NW India · Sanukitoids · TTGs · Petrogenesis

1 Introduction

The oldest stable lithospheric units, cratons, act as nuclei of Earth's continental crust and provide a snapshot of the processes related to Earth's early differentiation, recorded in the crust as old as ca. 4.03 Ga (Kamber and Tomlinson 2019; Stern and Bleeker 1998; Bowring and Williams 1999; Iizuka et al. 2006). These cratons host the Archean crust, which occupies only 7% of the exposed Earth's continental crust, while the rest has been decimated through crustal reworking and recycling processes that have acted for a period of over 3.5 billion years (Bowring and Williams 1999; Nutman 2006; Hawkesworth et al. 2010). The most widely accepted paradigm regarding the evolution of the continental crust suggests its formation from a mafic protolith that evolved to produce the oldest felsic rocks on Earth (Kemp et al. 2010; Dhuime et al. 2015; Tang et al. 2016; Rollinson 2017; Windley et al. 2021). Nevertheless, contention still prevails regarding the time of generation, the volume of the crust generated, and evolution of the early-formed crust through time (Hawkesworth et al. 2010; Moyen 2011; Condie 2018).

In the early Archean, the dominant crustal component consisted of Na-rich felsic rocks of the tonalite–trondhjemite–granodiorite (TTG; Jahn et al. 1981) affinity, generated by the melting of hydrous metabasite at variable

Supplementary Information The online version contains supplementary material available at https://doi.org/10.1007/s11631-024-00749-4.

✉ Parampreet Kaur
param.geol@gmail.com

[1] Department of Geology, Panjab University, Chandigarh, India

depths (Glikson 1979; Martin et al. 2005; Moyen and Martin 2012; Kendrick et al. 2024). During the Neoarchean Era (2.8–2.5 Ga), the Earth experienced rapid crustal growth due to large-scale melting events, leading to the diversification of early continental crust (e.g. Condie et al. 2009). There was a transition from Na-rich TTGs to more K-rich and large-ion lithophile (LILE)-enriched granitoids and sanukitoids (Sylvester 1994; Heilimo et al. 2011; Laurent et al. 2014). The timeline and extent of these changes varied across different cratons, but they generally followed a trend of a gradual increase in K-rich granitoids during the Neoarchean, marking the final phase of craton stabilization globally (Condie 1981; Heilimo et al. 2011; Martin 1993; Moyen et al. 2003; Laurent et al. 2014).

This transition indicates a shift in plate tectonic mechanisms from an Accretionary-style cycle to the modern Wilson-style cycle (Windley et al. 2021 and references therein) and also points to significant interactions between the mantle and crust. However, the origin and geodynamic processes responsible for this geochemical transition and tectonic shift remain contentious (Sun et al. 2024 and references therein). For example, questions persist about whether the older, less fertile TTGs could have produced large volumes of Neoarchean K-rich granitoids (Rollinson et al. 2024), whether the K- and LILE-enrichment resulted from partial melting of crust or a pre-metasomatized mantle (Wan et al. 2012; Sun et al. 2024), or whether K-rich granitoids were generated in active continental margins or formed by delamination of thickened crust (Zhao et al. 2008; Hu et al. 2019). Therefore, deciphering the geochemical signatures, petrogenesis and tectonic regime of Neoarchean granitoids is crucial for understanding the geodynamic evolution of Earth's crust during this time (Rollinson 2017).

In the northwestern part of India, the Aravalli orogen preserves one such cratonic nucleus, the Aravalli–Banded Gneissic Complex (BGC), which is mostly overlain by the supracrustal metasedimentary rock units of the late Paleoproterozoic Aravalli Supergroup (Roy and Jakhar 2002). A multitude of geochronological methods has deciphered the Archean antiquity (3.54–2.50 Ga: Kaur et al. 2019a, 2021 and references therein) of the Aravalli–BGC. Despite the availability of adequate geochronological data, systematic whole-rock geochemical and mineralogical investigations are lacking, which hinders the robust characterization of the granitoids in this terrane. This has led to their debatable status regarding their Archean or post-Archean lineage, particularly for some of the grey gneisses of the southern Aravalli–BGC terrane. This in turn restricts our understanding about the regional crustal evolution of the Aravalli orogen.

A case in point is the Jaisamand pluton around Udaipur city (Fig. 1), where the Jaisamand granitoids are thought to be associated with the metasedimentary rock units of the Aravalli Supergroup. The field and preliminary petrographic investigations suggested that these granitoids are post-Archean, as they intrude the rocks of the late Paleoproterozoic Aravalli Supergroup (Heron 1953; Gupta et al. 1997). Moreover, Shekhawat et al. (2001) proposed that the Jaisamand granitoids are intrusive into the Lower Aravalli sequence, and thus form the basement for the overlying rocks of the Upper Aravalli sequence. In contrast, Roy and Jakhar (2002) based on the occurrence of an unconformable surface between the basement and cover sequence, suggested that the Jaisamand granitoids acted as an Archean basement for the entire cover sequence of the Aravalli Supergroup. Therefore, the stratigraphic status of the Jaisamand pluton has been a matter of debate. To resolve this contentious issue, it is important to evaluate the nature of the Jaisamand granitoids through integrated field, petrographic and whole-rock geochemical investigation, which is the prime aim of this study. The application of these data unravels a unique and perhaps coeval spatial association of the Neoarchean TTGs and sanukitoids in a single pluton of the southern Aravalli–BGC. Our results also highlight the importance of carefully identifying the metasomatically altered Archean granitoids before characterizing and considering them for any petrogenetic interpretations.

2 Geological setting

Peninsular India has been divided into two major blocks: the North Indian Block (NIB) and the South Indian Block (SIB), which are separated by the Central Indian Tectonic Zone (CITZ), trending ENE–WSW (Fig. 1a; Naqvi and Rogers 1987; Jain et al. 1991; Eriksson et al. 1999; Acharyya 2003). In the northwestern part of NIB, the Aravalli orogen, a NNE–SSW-trending belt of ~ 700-km-long mountain belt, extends from Delhi in the north through mostly Rajasthan to the northern parts of Gujarat. The western margin of the orogen is marked by the Phulad Shear Zone separating it from the Neoproterozoic Marwar Block, while the eastern margin is marked by the Great Boundary Fault separating it from the late Paleoproterozoic–early Neoproterozoic Vindhyan Basin (Fig. 1b).

In the Aravalli orogen, the Aravalli–BGC (3.54–2.50 Ga; Gopalan et al. 1990; Wiedenbeck et al. 1996; Roy and Kröner 1996; Kaur et al. 2019a, 2021, 2023a) acts as an Archaean basement for the overlying three Proterozoic supracrustal units: the Aravalli Supergroup (< 2.45–1.60 Ga; McKenzie et al. 2013; Wang et al. 2019; Kaur et al. 2022), the North Delhi Supergroup (< 2.30–1.71 Ga; Kaur et al. 2011, 2013; Wang et al. 2017), and the South Delhi Supergroup (< 1.20–1.05 Ga; McKenzie et al. 2013; Wang et al. 2017; Kaur et al. 2023b). Based on the areal extent, the Aravalli–BGC has been demarcated into three domains (Kaur et al. 2021): the northern sector (region north of Jaipur), the

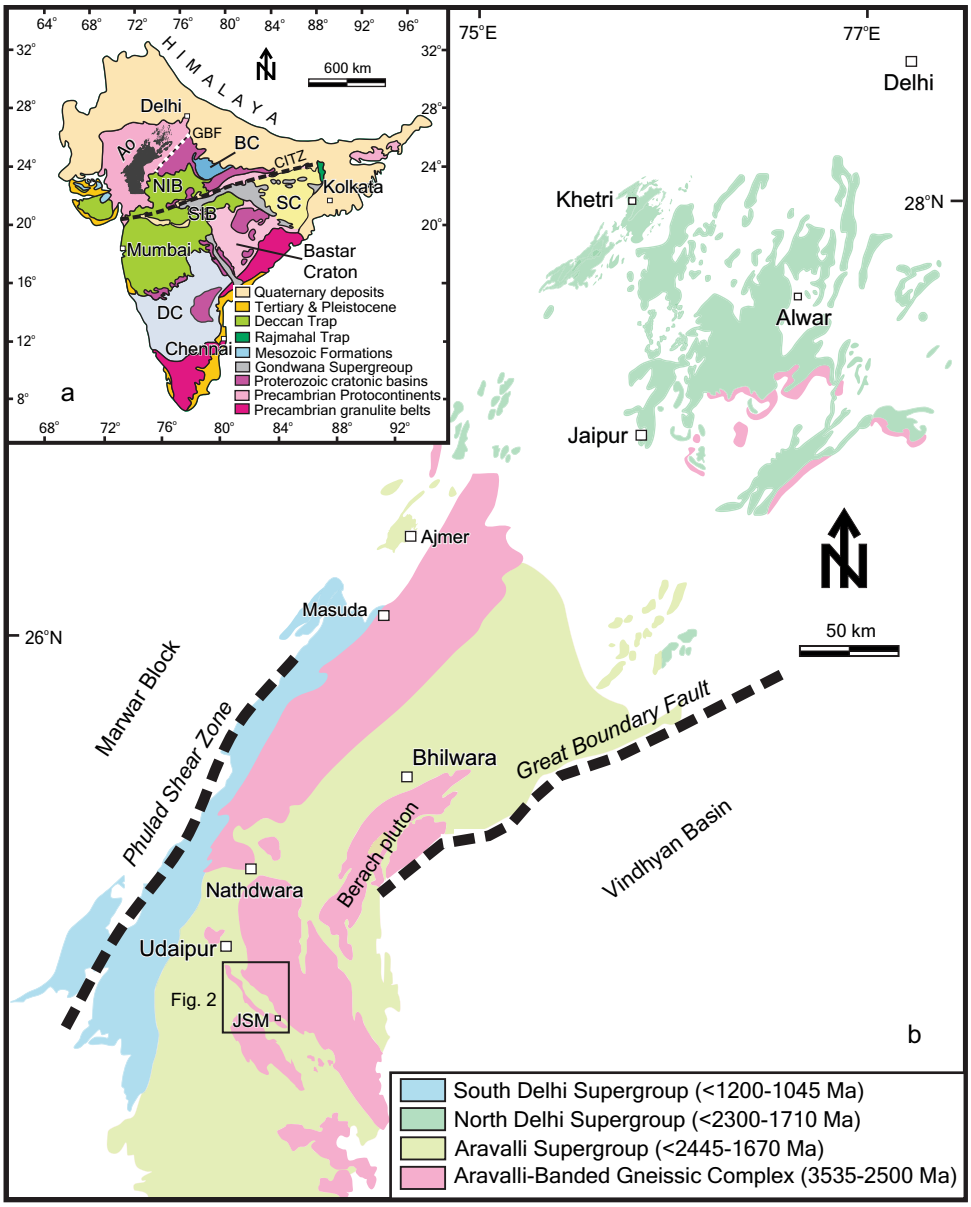

Fig. 1 **a** The broad divisions of tectonic blocks within India (Roy 2012); **b** regional geological map of the Aravalli orogen, NW India, along with major Precambrian stratigraphic units and location of the study area (compiled from Gupta et al. 1997; Roy and Jakhar 2002; Kaur et al. 2015, 2017). *Ao* Aravalli orogen, *BC* Bundelkhand Craton, *CITZ* Central Indian Tectonic Zone, *DC* Dharwar Craton, *GBF* Great Boundary Fault, *JSM* Jaisamand, *NIB* North Indian Block, *SC* Singhbhum Craton, *SIB* South Indian Block

central sector (region between Jaipur and Nathdwara), and the southern sector (region south of Nathdwara).

The southern Aravalli–BGC constitutes biotite-bearing-TTG gneisses, amphibolites, metasedimentary rocks, K-rich granitoids, and rare ultramafic rocks (Kaur et al. 2024a and references therein). The biotite-bearing TTG gneisses are typically gray with gneissic banding, and are largely intruded by K-rich granitoids and amphibolites (Roy and Jakhar 2002). These granitoids occur either within the TTG gneisses or as inliers surrounded by metasedimentary rocks of the Aravalli Supergroup (Roy and Jakhar 2002). The oldest TTG emplacement took place at ca. 3310 Ma, followed by a ca. 2828 Ma phase of mafic magmatism, emplacement of Neoarchean TTGs (2565–2550 Ma), sanukitoids (ca. 2540 Ma), potassic granitoids (2560–2500 Ma), and subsequent metamorphic events at ca. 2450 Ma and ca. 520 Ma (Gopalan et al. 1990; Wiedenbeck and Goswami 1994; Wiedenbeck et al. 1996; Roy and Kröner 1996; Kaur et al. 2019a).

The Jaisamand pluton forms a part of the southern Aravalli–BGC and is exposed 15 km SE of Udaipur (Figs. 1, 2). It occurs as a NW–SE-oriented elongated body, and is about 45 km long with varying widths of 0.5–3 km. The pluton extends from Dakankotra in the NW through Jaisamand town to Kherad in the SE. The metasedimentary rock units of the Upper Aravalli Group surround the Jaisamand granitoid body (Fig. 2). The eastern and northwestern flanks of the pluton are demarcated by stromatolitic- and phosphatic-dolomites, phyllites and conglomerates (Debari Formation), while the southwestern margin of the same is shared with

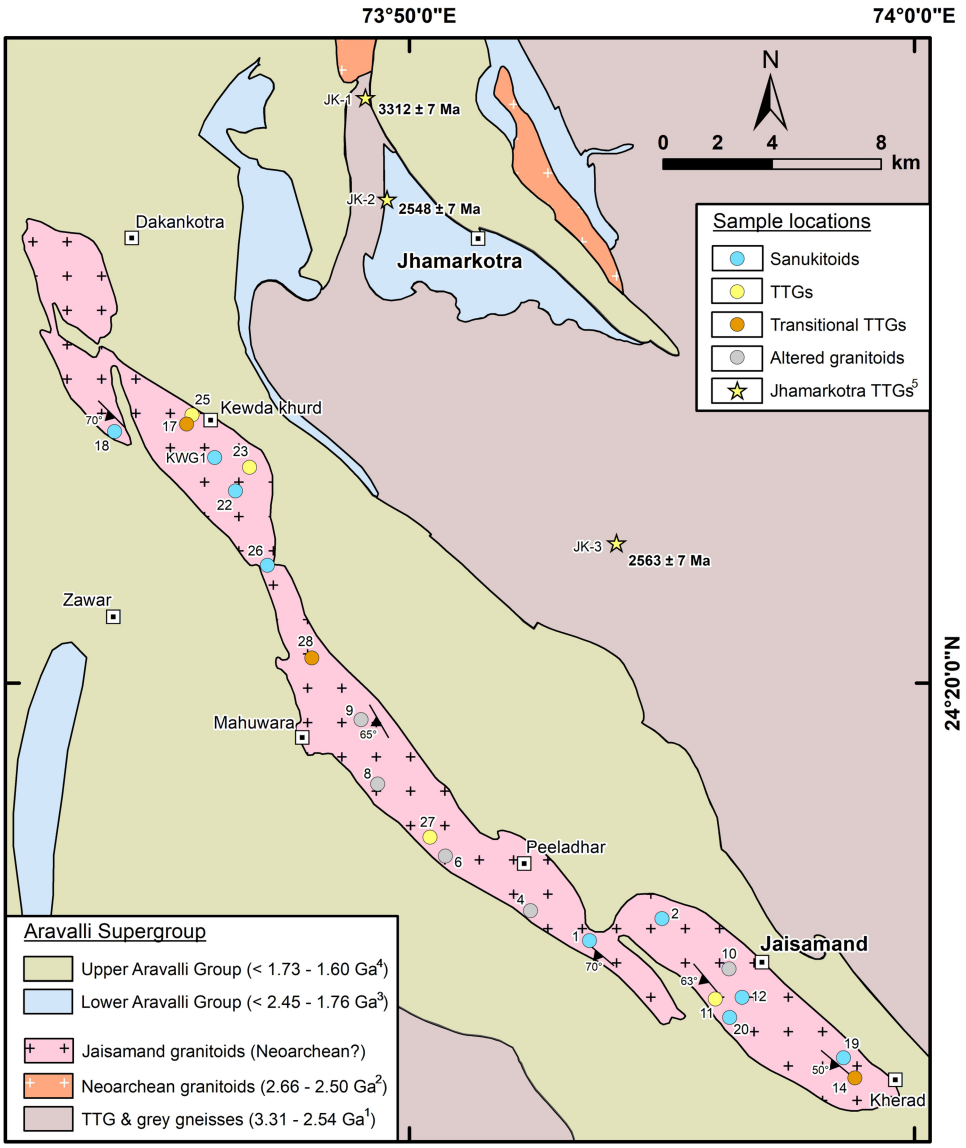

Fig. 2 Geological map of the Jaisamand granitoids and surrounding metasedimentary rock units of the Aravalli Supergroup along with sample locations (modified after Gupta et al. 1997). *Source of age data*: *1* Gopalan et al. (1990), Roy and Kröner (1996) and Kaur et al. (2019a); *2* Roy and Kröner (1996), Wiedenbeck et al. (1996) and Kaur et al. (2019a); *3* McKenzie et al. (2013) and Wang et al. (2019); *4* McKenzie et al. (2013), Wang et al. (2019) and Kaur et al. (2022); *5* Kaur et al (2019a)

phyllites and metagraywackes (Udaipur Formation; Gupta et al. 1997). The rocks of the Aravalli Supergroup reveal peak metamorphic conditions at 300–700 MPa/400–670 °C (Sharma 1988; Hahn et al. 2020; Wiszniewska et al. 2020).

3 Analytical techniques

3.1 Mineral chemistry

Minerals, such as plagioclase, biotite, microcline, epidote, and chlorite were analyzed for major and minor elements including Cl and F from ten representative samples of the granitoids, using a microprobe. Electron probe microanalyses (EPMA) were carried out at the Advanced Facility for Microscopy and Microanalysis, Indian Institute of Science, Bengaluru, India. The diamond polished sections were coated with 20-nm-thin layer of carbon using Quorum carbon coater 150R. A JEOL JXA 8230 electron probe microanalyzer was operated with inbuilt JEOL EPMA software at a voltage of 15 kV and current of 12 nA with tungsten filament source for generation of the electron beam from the electron gun and a probe diameter of about 3 µm. Natural silicate minerals used as standards were: orthoclase for K_2O, diopside for CaO, fluorite for F, Y-Al-garnet for Al_2O_3, quartz for SiO_2, hematite for FeO, Cr-oxide for Cr_2O_3, rutile for TiO_2, rhodonite for MnO, willemite for ZnO, albite for Na_2O, olivine for MgO, and tugtupite for Cl. During the initial spotting and probing of the mineral spots, simultaneous backscattered images (BSE) were taken by the EPMA instrument. The routine calibration, data acquisition, and quantification were performed using the inbuilt JEOL EPMA software, while the processing of the data was carried out using online CalcZAF/standard software.

3.2 Whole rock geochemical analysis

Twenty-one representative samples of the Jaisamand pluton were processed for whole-rock geochemical analyses, using the facilities at Panjab University, Chandigarh. The methods of the sample preparation are same as mentioned in Kaur et al. (2024b). The major and trace element analyses (package: WRA4B2 + 4Litho) were obtained from Activation Laboratories, Ontario, Canada, using a fusion method with a flux of lithium metaborate and lithium tetraborate. The details of analytical methods are discussed in Kaur et al. (2019b) or given at www.actlabs.com.

4 Results

4.1 Field characteristics and petrography

The rocks of Jaisamand pluton occur as isolated small mounds to low-lying outcrops, mostly surrounded by anthropogenic activities (Fig. 3a). Based on their mineralogical and geochemical characteristics (see below), the Jaisamand granitoids can be broadly classified into four types: sanukitoids, TTGs, transitional TTGs, and altered granitoids. The TTGs and sanukitoids are dark to light gray, medium- to coarse-grained and well-foliated (Fig. 3b), with minimal variations in textural characteristics and degree of deformation among these rocks. The altered granitoids, however, show a subdued foliation (Fig. 3c) due to the dissolution of mafic phases (see below). Furthermore, no cross-cutting relationships among various granitoids are discernible in the Jaisamand pluton. In some places, the granitoids show signs of shearing, indicated by the pinching of the quartz veins and the development of strong foliation in the adjacent granitoid domain (Fig. 3d). Overall, the foliation in these rocks strikes NW–SE with SW dips ranging from 50° to 70° (Fig. 2). The granitoids show an intrusive relationship with the surrounding metabasites (Fig. 3e).

4.1.1 Sanukitoids

The foliation in the sanukitoids is mostly defined by biotite (Fig. 3f). Plagioclase (34–53 vol%), quartz (18–30 vol%; excluding sample 2JMG20: ~ 9 vol%) and biotite (5–28 vol%) are the dominant phases, and epidote (1–9 vol%), apatite, zircon, titanite, Fe-Ti oxides, and tourmaline occur as accessory minerals along with secondary white mica (0.5–10 vol%; Table 1). In the ternary QAP plot of Streckeisen (1976), these rocks are mostly classified as tonalite (M = 17.5–41.0 vol%; Table 1; M = mafic and related minerals = volume % of mica + accessory minerals + epidote), except for sample 2JMG20, which is a quartz diorite (Fig. 4).

The plagioclase is variably altered to epidote, sericite, and/or calcite, with most of the crystals showing relatively clean cores and rims with effects of sericitization and saussuritization (Fig. 3f). In places, the plagioclase twin lamellae are bent and displaced, showing the effect of deformation (Fig. 3g). The composition of plagioclase varies from albite to oligoclase ($An_{1.8–19.6}$; $n = 35$; Fig. 5a; Table S1), and, in sample JMG2, the plagioclase is exclusively oligoclase.

Biotite occurs as a major mafic phase, mostly as subhedral laths- to tabular-shaped flakes, which are interstitial to plagioclase and quartz (Fig. 3g). The mineral is largely associated with epidote, apatite, zircon, titanite, and Fe-Ti oxides (Fig. 3f, h). In places, incipient to complete alteration of biotite to chlorite and/or muscovite is observed (Fig. 3g). Biotite is phlogopite to annite in composition with X_{Fe} [$X_{Fe} = Fe^t/(Fe^t + Mg)$] varying between 0.45 and 0.52 (Fig. 5b; Table S2). It shows a wide variation in F contents (0.00–0.27 wt%), but relatively homogeneous Cl abundances (0.00–0.04 wt%; Table S2). In the discrimination diagram of Abdel-Rahman (1994), the biotite shows its affinity with calc-alkaline orogenic suites (C-type; Fig. 5c).

Epidote occurs mostly as subhedral to euhedral, prismatic to fine granular aggregates (Fig. 3h). The prismatic epidote is colorless to pale yellow, occasionally zoned, and is associated with unaltered biotite (Fig. 3h, i). In places, the presence of zonation, an allanite-rich core surrounded by epidote, and its partial enclosure in biotite and embayed boundaries in contact with plagioclase and quartz are the typical features of magmatic epidote (Fig. 3j; Zen and Hammarstrom 1984; Schmidt and Thompson 1996; Schmidt and Poli 2004). In contrast, the fine granular aggregates occurring as inclusions in plagioclase show blue to lemon yellow interference colors and are secondary zoisite and clinozoisite, respectively (Fig. 3I). The < 0.2 wt% TiO_2 abundance in magmatic epidote (TiO_2 = 0.01–0.13 wt%; Table S3) further support their magmatic origin (Evans and Vance 1987). The cores of the mineral are relatively iron-poor [$X_{Ep\text{-}core}$ = 0.52–0.63; $X_{Ep} = Fe^{3+}/(Fe^{3+} + Al + Cr^{3+} - 2)$] with pistacite contents [$Ps = (Fe^{3+}/(Fe^{3+} + Al) \times 100$] ranging from 15 to 19 mol% (Table S3), while the rims are relatively iron-rich ($X_{Ep\text{-}rim}$ = 0.69–0.76) with higher Ps of 21–25 mol% (Fig. 6a; Table S3). The pistacite (Ps) contents of the core are relatively low than the recommended values for magmatic epidote (25–33 mol%; Liou 1973; Tulloch 1986; Zen 1988). Nevertheless, textural evidence is more reliable than the compositional criteria to delineate the magmatic nature of epidote (Schmidt and Poli 2004). The magmatic epidote with lower Ps contents has also been reported: for example, epidote in the Galiléia batholith (Brazil) shows Ps contents of 9.3–22.2 mol% (Narduzzi et al. 2017), and epidote in the Olho d'Água pluton (Brazil) shows Ps = 17–26 mol% (Siqueira et al. 2021 and references therein).

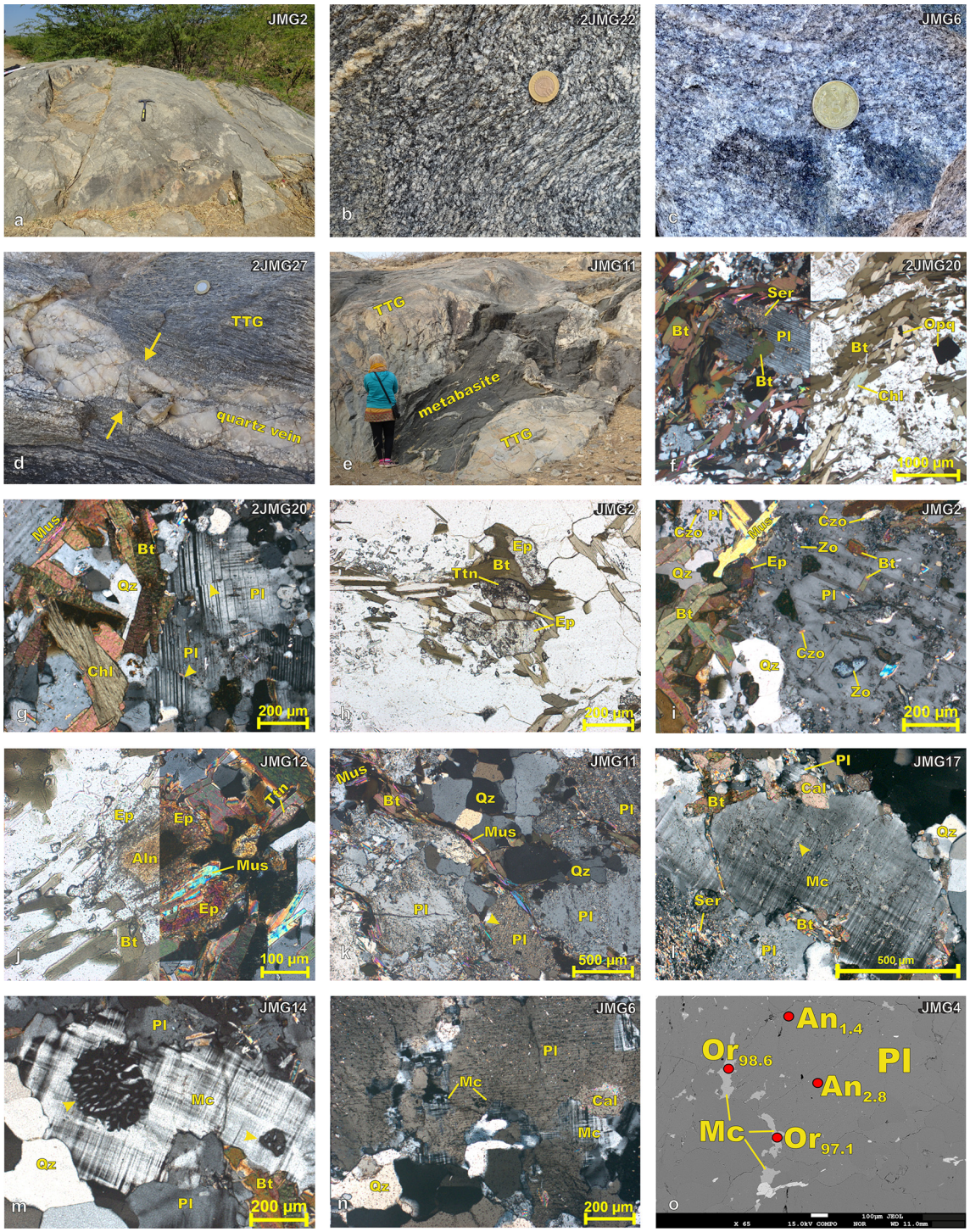

Titanite occurs as subhedral to anhedral aggregates either as partially enclosed or as inclusions within the biotite. In places, titanite is also associated with epidotes and/or Fe–Ti oxides (Fig. 3h).

Chlorite occurs as subhedral laths, mostly with biotite and/or Fe–Ti oxides. The mineral shows anomalous brown to violet/blue interference colors (Fig. 3g). The analyzed chlorite spots show a type-I trioctahedral, Mg-chlorite composition with X_{Mg} [X_{Mg} = Mg/(Mg + Fe^t)] values between 0.59 and 0.60 (Fig. 6b; Table S4).

4.1.2 TTGs

The TTGs show a well-developed foliation (Fig. 3d, e) defined by biotite and/or muscovite (Fig. 3k). The major minerals include plagioclase (44–53 vol%), quartz (26–33

◂**Fig. 3** Representative field photographs and photomicrographs of the Jaisamand sanukitoids (**a**, **b** and **f–j**), TTGs (**d**, **e**, and **k**), transitional TTGs (**l–m**) and altered granitoids (**c** and **n–o**). **a** topographically low-lying sanukitoid outcrop (length of hammer = 11.5 inch); **b** sanukitoids showing preferred orientation of biotite, defining a strongly developed foliation (coin diameter = 27 mm); **c** altered granitoids with less abundant biotite, defining a subdued foliation (coin diameter = 25 mm); **d** pinching of quartz vein (*yellow arrow*) and development of a strong foliation in the deformed TTG (coin diameter = 27 mm); **e** intrusive relationship of the TTGs with the metabasite (height of the person = 160 cm); **f** hypidiomorphic–granular texture, foliation, alteration of plagioclase to sericite and alteration of biotite to chlorite; **g** displaced albite twin lamellae (*yellow triangles*) in plagioclase, indicating effect of deformation, and interstitial biotite showing its alteration to chlorite and muscovite; **h** association of biotite with epidote and titanite; **i** alteration of plagioclase to zoisite and clinozoisite; **j** allanite core with epidote rim, showing embayed margin in contact with quartz and plagioclase; **k** foliation defined by biotite and muscovite, an overall hypidiomorphic-granular texture, less altered plagioclase with relatively clean core and more altered plagioclase showing sericitization along the albite twin lamellae (*yellow triangle*); **l** tartan twinned microcline showing albite veins (*yellow arrow*) along with diffused grain boundary with adjoining plagioclase, and alteration of plagioclase to sericite and calcite, **m** myrmekitic texture (*yellow triangle*) in microcline; **n** microcline islands in the plagioclase with parallelism between the albite and the tartan twin planes and formation of secondary calcite and **o** BSE image showing relics of microcline in plagioclase along with their An and Or contents. Photomicrographs 3f and j are under both one nicol and crossed nicols, 3 h is under one nicol and all others are under crossed nicols. Mineral abbreviations are after Whitney and Evans (2010)

vol%), and biotite (10–15 vol%). The accessory minerals are epidote (1–8 vol%), zircon, apatite, titanite, Fe-Ti oxides, tourmaline, and secondary white mica (0–4 vol%; Table 1). The TTGs occupy the tonalite field in the ternary QAP plot (Fig. 4).

Plagioclase is variably altered and deformed as observed in the sanukitoids (Fig. 3k). They are albite to oligoclase ($An_{1.7–19.1}$; $n = 23$; Fig. 5a; Table S1) in composition.

The mode of occurrence, association, and alteration features of biotite are the same as observed in the sanukitoids. They are, however, annite in composition with X_{Fe} varying from 0.50 to 0.54 (Fig. 5b; Table S2). The variations and abundances of halogens are broadly same as those in the sanukitoids (F = 0.00 wt%–0.28 wt% and Cl = 0.04 wt%–0.05 wt%; Table S2). Like sanukitoids, the biotite is typical of calc-alkaline suites (Fig. 5c).

Epidote shows similar textural features for magmatic and secondary ones as those in the sanukitoids.

4.1.3 Transitional TTGs

The transitional TTGs are megascopically and microscopically similar to the sanukitoids and TTGs. The major phases include plagioclase (40–47 vol%), quartz (25–28 vol%), K-feldspar (6–12 vol%), and biotite (7–10 vol%). The accessory phases are epidote (1–3 vol%), titanite, zircon, apatite, Fe-Ti oxides, and secondary white mica (1–8 vol%; Table 1). In contrast to the sanukitoids and TTGs, the transitional TTGs occupy the granodiorite field in the ternary QAP plot (Fig. 4) because of the occurrence of K-feldspar.

The textural features exhibited by various major and accessory phases are similar to those observed in the sanukitoids and TTGs. Plagioclase is oligoclase ($An_{13.8–22.7}$; $n = 10$; Fig. 5a; Table S1), and biotite is annite with slightly higher X_{Fe} ($X_{Fe} = 0.55–0.56$) values than those in the TTGs (Fig. 5b; Table S2), and is typical of calc-alkaline suites (Fig. 5c).

The K-feldspar mostly occurs as subhedral tabular, tartan twinned microcline–perthite, showing a diffused grain boundary and a myrmekitic texture in association with plagioclase (Fig. 3l, m). Compositionally, the mineral shows a limited variation with $Or_{88.9–95.2}$ ($n = 7$; Fig. 5a; Table S5). The cores and rims of the magmatic epidote show similar variations for X_{Ep} values, and Ps contents as those observed in the sanukitoids (Fig. 6a; Table S3).

4.1.4 Altered granitoids

In the Jaisamand pluton, some of the granitoids show effects of metasomatism and are classified as altered granitoids. These granitoids are gray, whitish gray to white, and feebly foliated due to lesser abundances of the mafic phases (Fig. 3c; Table 1). In these rocks, most of the microcline occurs as islands within the plagioclase, and the twin planes of the latter mineral show continuity with the tartan twinning pattern of microcline (Fig. 3n, o), suggesting transformation of microcline to plagioclase during a phase of Na-metasomatism. The major minerals include plagioclase (36–58 vol%), quartz (28–38 vol%), microcline (0–6 vol%, except in sample JMG9, microcline = 18 vol%), and biotite (3–8 vol%), along with accessory zircon, Fe–Ti oxides, titanite, apatite, epidote, allanite, and secondary white mica and chlorite (Table 1). Notably, the estimated modal abundances of accessory (1–1.5 vol%) and mafic phases (biotite = 3–8 vol%) are lower in these granitoids (Table 1). Most of the analyzed plagioclase spots have An contents ≤ 5 (see below), and therefore, in the ternary QAP plot, these granites are classified as alkali feldspar granites (Streckeisen 1976), except for sample JMG8 (An ≥ 5 and K-feldspar absent) which falls in the tonalite field (Fig. 4).

Plagioclase occurs as subhedral tabular and sometimes with bent twin lamellae, showing variable effects of alteration to calcite, sericite, and epidote (Fig. 3n). The mineral is virtually pure albite ($An_{1.2–5.9}$; $n = 34$) except in JMG8 where albite to oligoclase composition is observed ($An_{6.8–16.2}$; $n = 11$; Figs. 5a, 3o; Table S1). The relict microcline islands show higher orthoclase composition than those in the TTGs ($Or_{94.7–98.6}$; $n = 22$; Figs. 5a, 3o; Table S5). Biotite is phlogopite to annite in composition with an X_{Fe}

Table 1 Estimated modal analyses (in volume percent) for the Jaisamand granitoids

Rock type	Sanukitoids									TTGs	
Sample no.	KWG1[a]	JMG1[a]	JMG2[a]	JMG12[a]	JMG18[a]	2JMG19[a]	2JMG20[b]	2JMG22[a]	2JMG26[a]	JMG11[a]	2JMG23[a]
Quartz	23	22	26	26	30	24	9	18	22	33	30
Plagioclase	46	53	47	52	38	34	45	48	45	48	44
K-feldspar	–	–	–	4	–	–	–	–	–	–	–
Biotite	15	18	15	11	5	20	25	28	12	10	11
Muscovite	0.5	3	2	2	10	5	4	–	5	4	–
Epidote	9	1	6	3	7	9	4	3	6	1	8
Calcite	1	1	1	0.5	–	1	–	–	2	0.5	–
Chlorite	3.5	–	1	–	7	1	5	1	2	0.5	2
Acc. min	2	2	2	1.5	3	6	8	2	6	3	5
M	26.5	24.0	25.0	17.5	25.0	40.0	41.0	33.0	29.0	18.0	24.0

Rock type	TTGs		Transitional TTGs			Altered granitoids				
Sample no	2JMG25[a]	2JMG27[a]	JMG14[c]	JMG17[c]	2JMG28[c]	JMG4[d]	JMG6[d]	JMG8[a]	JMG9[d]	JMG10[d]
Quartz	26	26	25	28	27	30	28	38	34	38
Plagioclase	53	44	47	41	40	54	58	44	40	36
K-feldspar	–	3	11	6	12	4	6	–	18	1
Biotite	12	15	10	10	7	5	3	8	5	4
Muscovite	2	2	1	7	8	1	1	5	1	15
Epidote	3	4	3	1	2	2	2	2	1	0.5
Calcite	–	3	–	2	1	–	–	1	–	2
Chlorite	1	0.5	–	4	0.5	3	0.5	0.5	–	2
Acc. min	3	2.5	3	1	2.5	1	1.5	1.5	1	1.5
M	20.0	23.5	17.0	19.0	19.5	9.0	7.5	16.5	8.0	18.0

[a]Tonalite [b]Quartz diorite [c]Granodiorite [d] Alkali feldspar granite; *Acc. min* accessory minerals, *M* mafic and related minerals = volume % of mica + accessory minerals + epidote

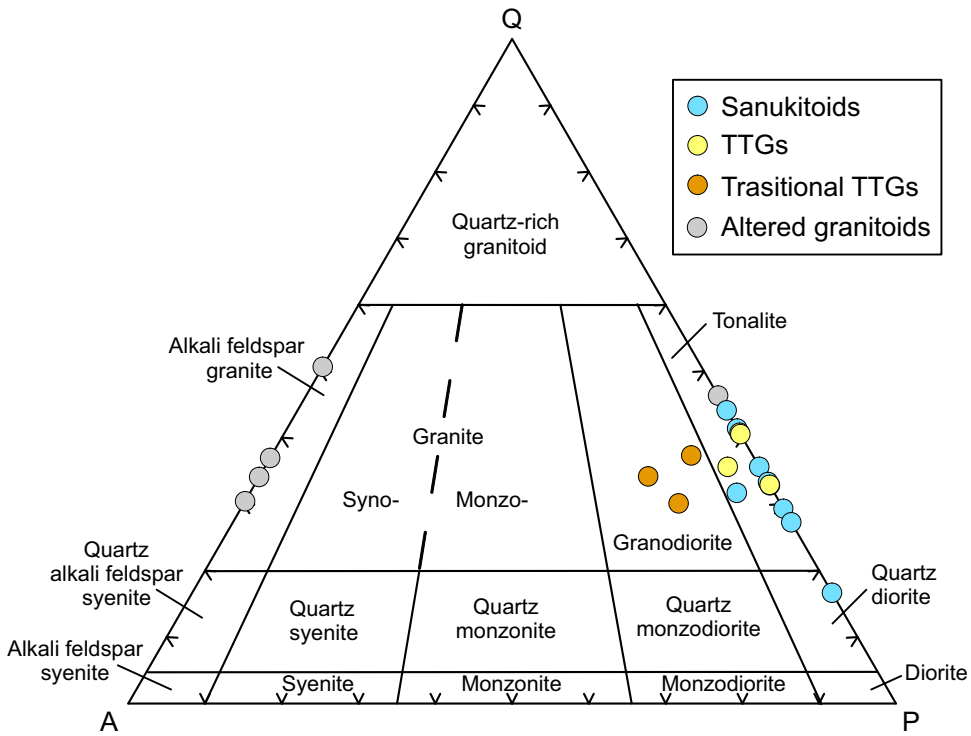

Fig. 4 Ternary QAP (quartz—alkali feldspar—plagioclase) modal classification diagram (Streckeisen 1976) for the Jaisamand granitoids

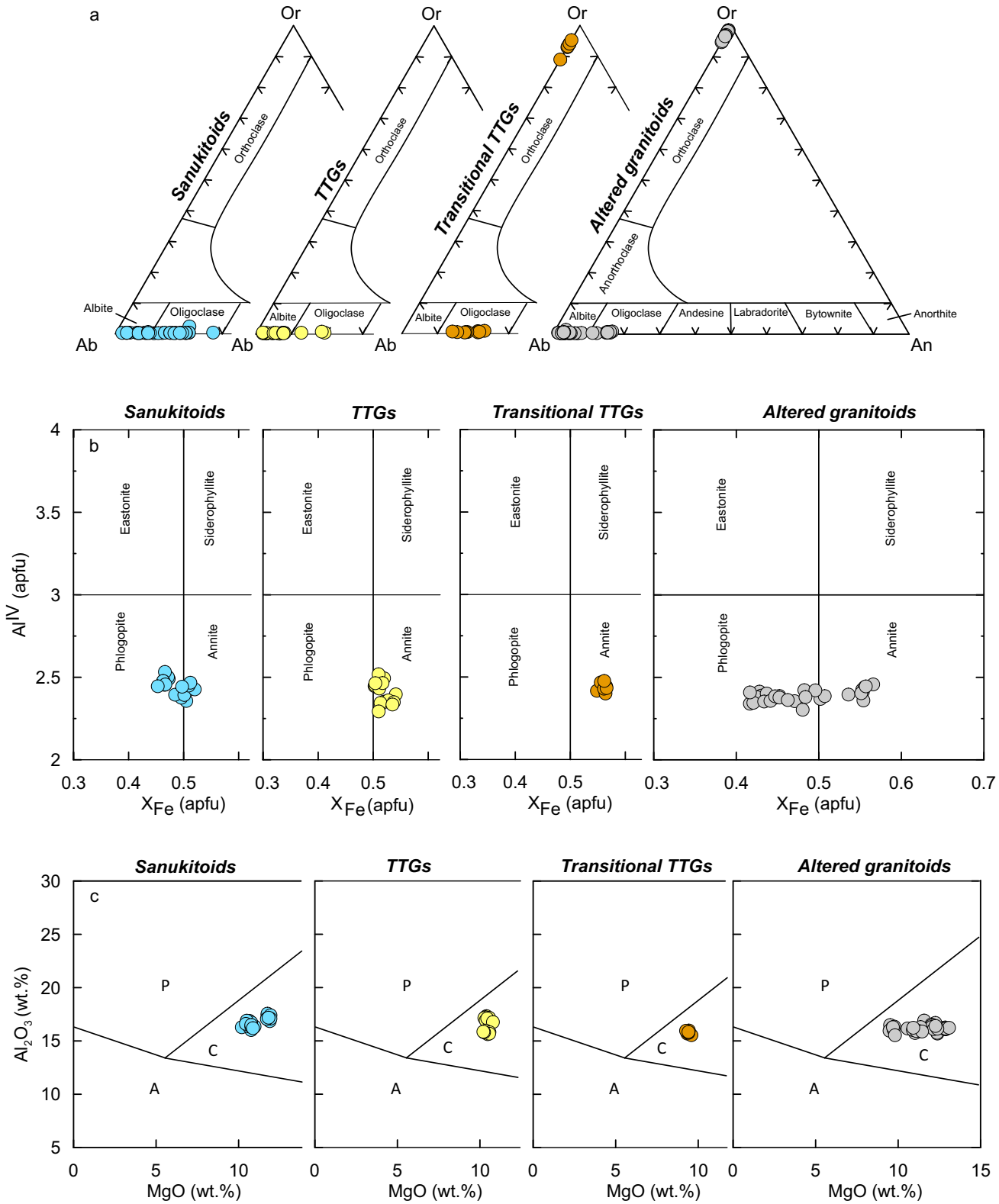

Fig. 5 **a** Or–Ab–An diagram for feldspars (Deer et al. 2013); **b** X_{Fe} (apfu) [$=Fe^t/(Fe^t + Mg)$] versus Al^{IV} (apfu) diagram for biotite (Deer et al. 2013); and **c** MgO (wt%) versus Al_2O_3 (wt%) plot for biotite (Abdel-Rahman 1994). *apfu* atom per formula unit, *A* anorogenic alkaline suites, *C* calc-alkaline orogenic suites, *P* peraluminous (including S-type) suites

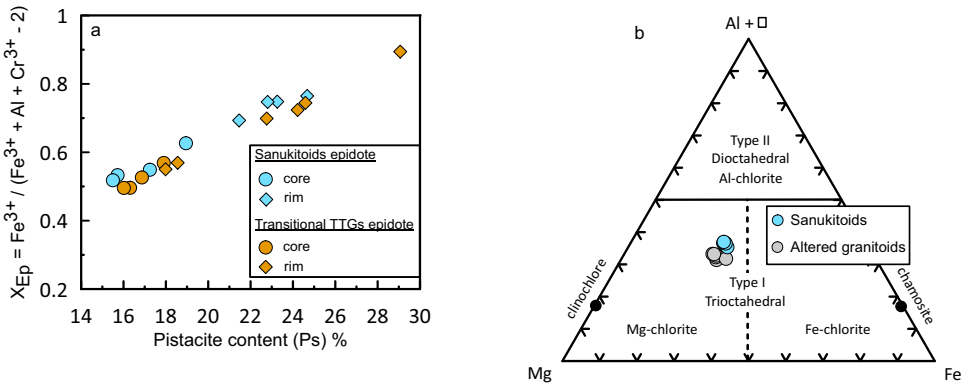

Fig. 6 **a** Ps [pistacite content, $Ps = Fe^{3+}/(Fe^{3+} + Al) \times 100$)] versus X_{Ep} diagram for epidote and **b** ternary (Al + □)–Mg–Fe diagram (Zane and Weiss 1998). □ (octahedral vacancy) = (12—∑ octahedral site), where ∑ octahedral site = (Al^{VI} + Ti + $Fe.^{t}$ + Mg + Mn)

value between 0.42 and 0.57 (Fig. 5b; Table S2), and halogens (Cl and F) in the mineral (F = 0.04–0.31 wt% and Cl = 0.00–0.06 wt%; Table S2) show overlapping abundances as those in the other granitoids. Chlorite is type-I trioctahedral, Mg-chlorite as observed in the sanukitoids but, compared to the latter, it shows slightly higher Mg-contents with X_{Mg} varying between 0.59 and 0.64 (Fig. 6b; Table S4).

4.2 Whole-rock geochemistry

4.2.1 Sanukitoids

The rocks show variable Si (SiO_2 = 55.7–67.1 wt%), Al (Al_2O_3 = 15.90–18.33 wt%), Ca (CaO = 2.11–4.84 wt%), K (K_2O = 1.90–3.30 wt%), Mg (MgO = 1.54–3.76 wt%), and Fe ($Fe2O3^{t}$ = 3.52–7.73 wt%) abundances (Table 2). They are characterized by low Na_2O/K_2O (1.26–2.45), but high ferromagnesian oxides (FM oxides: FeO^{t} + MgO + MnO + TiO_2 = 5.27–11.45 wt%), Mg# (44–50), Ba + Sr (823–1407 ppm), V (48–99 ppm), Cr (20–90 ppm), LREE [$(La/Yb)_N$ = 22.6–44.5, except samples JMG1 and 2JMG26, $(La/Yb)_N \leq 10.0$; Table 2], and moderately high $(Gd/Er)_N$ = 2.0–3.0 [except samples JMG1 and 2JMG26, $(Gd/Er)_N$ = 1.5]. Among these variations, the abundances of FM oxides, Na_2O/K_2O ratios, Mg#, MgO, Br + Sr, $(Gd/Er)_N$, and LREE are typical of late-Archean sanukitoids (Halla 2005; Halla et al. 2009; Martin et al. 2009; Heilimo et al. 2010; Laurent et al. 2014). Moreover, the classification diagrams of Archean granitoids and the plots of Berach and Masuda sanukitoids of the Aravalli–BGC also corroborate their sanukitoid affinity (Fig. 7a–c).

In the normative An–Ab–Or classification diagram of Barker (1979), the sanukitoids largely spread across the fields of tonalite, trondhjemite, and granodiorite, and fall in the field of Archean TTGs, away from the modern or post-Archean granitoids (Fig. 8a), which is also supported by the cationic K–Na–Ca diagram (Fig. 8b). The rocks are mostly calc-alkalic to alkali-calcic, magnesian, weakly peraluminous, and medium-K (calc-alkaline) in nature (Fig. 8c–f).

Based on chondrite-normalized REE patterns, the sanukitoids can be distinguished into two groups: (1) moderately fractionated REE group [$(La/Yb)_N \leq 10.0$; samples JMG1 and 2JMG26] with flat HREE patterns [$(Gd/Yb)_N$ = 1.9] and negative Eu anomalies (Eu/Eu* = 0.56–0.68; Fig. 9a; Table 2), and (2) highly fractionated REE group [$(La/Yb)_N$ = 22.6–44.5] with flat to depleted HREE patterns [$(Gd/Yb)_N$ = 2.2–3.2] and moderately negative to no Eu anomalies (Eu/Eu* = 0.74–1.06; Fig. 9a; Table 2). The overall REE patterns are mostly comparable to the average pattern of the high-HREE-Y TTG group (Moyen and Martin 2012; Laurent et al. 2024), except for two samples (JMG2 and 2JMG20) which show similarity with medium-HREE-Y TTG group (Fig. 9a). The REE patterns are also similar to those of the 2545–2540 Ma Masuda and Berach sanukitoids of the Aravalli–BGC. In the multi-element primitive mantle-normalized diagram, the Jaisamand sanukitoids show relatively high contents of LILE and LREE compared to those of high-field strength elements (HFSE), a feature typical of subduction-related magmas (Fig. 9b). Most of the sanukitoids show significant negative anomalies for Nb, Sr, P and Ti, and, overall, the patterns are remarkably similar to the average pattern of sanukitoids as defined by Halla et al. (2009), and are also comparable with the Masuda and Berach sanukitoids.

4.2.2 TTGs

These rocks compared to the sanukitoids (Table 2) show relatively high Si contents (SiO_2 = 66.8–71.9 wt%), Na (Na_2O = 4.65–6.65 wt%), and Na_2O/K_2O ratios (1.90–4.86), but low Al (Al_2O_3 = 14.30–15.52 wt%), Ca (CaO = 1.15–2.31 wt%), Mg (MgO = 1.02–1.77 wt%), Fe ($Fe_2O_3^{t}$ = 2.34–3.95 wt%), FM oxides (3.50–5.71 wt%), and Mg# (45–47). Moreover, the rocks are also characterized by relatively low Ba + Sr (516–1010 ppm), K (K_2O = 1.37–2.45 wt%), K_2O/Na_2O (0.21–0.53), (Gd/

Table 2 Whole-rock chemical compositions for the Jaisamand granitoids, NW India

Rock type	Sanukitoids									TTGs	
Sample no.	KWG1[a]	JMG1[a]	JMG2[a]	JMG12[a]	JMG18[a]	2JMG19[a]	2JMG20[b]	2JMG22[a]	2JMG26[a]	JMG11[a]	2JMG23[a]
Lat. (°N)	24°24′	24°14′	24°15′	24°13′	24°24′	24°12′	24°13′	24°23′	24°22′	24°13′	24°24′
	27.9″	54.1″	20.3″	46.7″	58.8″	34.9″	22.9″	48.4″	19.9″	44.9″	16.4″
Long. (°E)	73°46′	73°53′	73°54′	73°56′	73°44′	73°58′	73°56′	73°46′	73°47′	73°56′	73°46′
	8.5″	33.8″	59.9″	35.2″	09.5″	35.6″	20.5″	33.1″	11.2″	03.5″	49.9″
SiO_2 (wt%)	62.5	64.2	65.7	67.1	65.2	61.9	55.7	60.1	65.1	71.9	70.7
TiO_2	0.70	0.52	0.59	0.52	0.58	0.73	0.66	0.8	0.52	0.35	0.33
Al_2O_3	16.98	16.33	15.92	16.17	15.90	16.02	18.33	16.34	15.90	15.12	14.30
$Fe_2O_3^t$	5.41	4.00	4.35	3.52	4.80	5.93	7.73	6.31	4.67	2.34	2.52
MnO	0.07	0.05	0.06	0.04	0.05	0.07	0.08	0.06	0.06	0.03	0.03
MgO	2.16	1.91	1.87	1.54	2.11	2.34	3.76	3.15	1.83	1.02	1.05
CaO	4.84	2.75	3.54	2.57	2.79	4.10	2.11	2.78	3.07	1.73	1.15
Na_2O	4.30	5.13	4.58	5.25	4.66	3.97	4.79	4.86	3.89	4.97	4.76
K_2O	2.17	2.66	2.05	2.30	1.90	2.03	3.30	2.37	3.10	1.68	2.02
P_2O_5	0.28	0.43	0.21	0.20	0.21	0.32	0.03	0.31	0.20	0.10	0.12
LOI	1.27	1.59	1.01	1.14	1.58	1.11	1.72	1.95	2.20	0.94	1.53
Sum	100.7	99.6	99.8	100.4	99.8	98.5	98.2	99.0	100.5	100.1	98.5
Sc (ppm)	9	7	4	6	7	9	10	10	8	6	3
V	90	60	76	56	69	94	48	99	62	40	28
Cr	50	40	20	20	40	30	90	40	20	40	< 20
Ni	20	< 20	< 20	< 20	20	< 20	20	< 20	< 20	< 20	< 20
Zn	60	50	80	30	60	60	80	60	50	< 30	< 30
Ga	23	19	19	17	19	20	25	22	22	16	16
Rb	54	67	58	50	39	55	105	63	92	43	36
Sr	664	365	544	386	344	492	224	419	477	165	125
Y	16	31	9	13	14	14	8	15	26	16	9
Zr	201	155	161	180	201	213	263	217	181	139	120
Nb	8	9	4	8	7	4	14	5	7	8	2
Ba	743	999	612	808	898	620	599	505	543	516	885
Pb	10	7	10	12	6	7	11	9	18	14	< 5
Th	4.2	4.3	5.7	8.1	7.1	4	20.8	4.2	5.8	8.3	5.6
U	0.8	1	1	1.4	1.4	1.2	1.3	0.8	1.9	1.4	0.7
Hf	4.6	3.8	3.8	3.9	4.8	4.3	6.3	4.6	4.2	3.3	2.5
Ta	0.5	0.9	0.3	0.6	0.5	0.3	1.7	0.4	1	0.8	0.4
La	55.6	37.4	42.8	37.9	47.6	38.2	49.8	42	30.8	32.9	36.2
Ce	104	75.5	74.5	72.7	89.1	70.4	86.8	80.4	60.7	62	64.8
Pr	11.6	9.11	7.75	8.2	9.93	7.91	9.14	9.24	7.04	6.99	6.67
Nd	42.5	36.9	26.8	30.1	37.4	31	31.1	37.1	28	25.4	23.5
Sm	6.9	7.6	4	5.1	6	5.5	4.9	7	6.2	4.7	4.1
Eu	1.75	1.26	1.08	1.12	1.19	1.46	1.22	1.54	1.26	1.05	0.95
Gd	4.7	6.2	2.4	3.2	4	3.8	3	4.7	5.1	3.3	2.5
Tb	0.7	1	0.3	0.5	0.6	0.6	0.4	0.6	0.9	0.5	0.3
Dy	3.4	6.3	1.8	2.5	3	2.9	1.9	3.4	5	3.1	1.9
Ho	0.6	1.2	0.3	0.4	0.5	0.5	0.3	0.6	1	0.6	0.3
Er	1.7	3.3	0.9	1.3	1.4	1.4	0.8	1.5	2.8	1.7	0.8
Tm	0.23	0.45	0.14	0.17	0.18	0.19	0.11	0.2	0.37	0.24	0.11
Yb	1.5	2.7	0.9	1.2	1.1	1.1	0.8	1.2	2.2	1.5	0.8
Lu	0.22	0.36	0.16	0.17	0.17	0.16	0.13	0.16	0.31	0.25	0.11
∑ REE	235.4	189.3	163.8	164.6	202.2	165.1	190.4	189.6	151.7	144.2	143.0

Table 2 (continued)

Rock type	Sanukitoids									TTGs	
Sample no.	KWG1[a]	JMG1[a]	JMG2[a]	JMG12[a]	JMG18[a]	2JMG19[a]	2JMG20[b]	2JMG22[a]	2JMG26[a]	JMG11[a]	2JMG23[a]
$(Gd/Er)_N$	2.2	1.5	2.1	2.0	2.3	2.2	3.0	2.5	1.5	1.6	2.5
$(La/Yb)_N$	26.5	9.9	34.0	22.6	30.9	24.8	44.5	25.0	10.0	15.7	32.3
$(Gd/Yb)_N$	2.6	1.9	2.2	2.2	3.0	2.8	3.1	3.2	1.9	1.8	2.5
Eu/Eu*	0.93	0.56	1.06	0.84	0.74	0.97	0.96	0.81	0.68	0.81	0.90
Na_2O/K_2O	1.98	1.93	2.23	2.28	2.45	1.95	1.45	2.05	1.26	2.96	2.36
K_2O/Na_2O	0.50	0.52	0.45	0.44	0.41	0.51	0.69	0.49	0.80	0.34	0.42
Mg#	44	49	46	46	47	44	49	50	44	46	45
FM oxides	7.79	6.08	6.43	5.27	7.07	8.48	11.45	9.69	6.36	3.50	3.56
$FeO^T + MgO$	7.03	5.51	5.78	4.71	6.43	7.68	10.72	8.83	6.03	3.13	3.32
Ba + Sr	1407	1364	1156	1194	1254	1112	823	924	1020	681	1010
La/Sm	8.06	4.92	10.70	7.43	7.93	6.95	10.16	6.00	4.97	7.00	8.83
Nb/Sm	1.16	1.18	1.00	1.57	1.17	0.73	2.86	0.71	1.13	1.70	0.49
U/Th	0.19	0.23	0.18	0.17	0.20	0.30	0.06	0.19	0.33	0.17	0.13
Th/Yb	2.80	1.59	6.33	6.75	6.45	3.64	26.00	3.50	2.64	5.53	7.00
Ba/La	13.36	26.71	14.30	21.32	18.87	16.23	12.03	12.02	17.63	15.68	24.45
Nb/Nb*	0.12	0.17	0.06	0.11	0.09	0.08	0.10	0.09	0.12	0.11	0.03
Pb/Pb*	3.02	2.80	4.36	5.15	2.12	3.11	4.10	3.46	9.13	7.05	-
ASI	0.97	1.07	1.01	1.06	1.11	1.04	1.21	1.10	1.07	1.17	1.21

Rock type	TTGs		Transitional TTGs			Altered granitoids				
Sample no.	2JMG25[a]	2JMG27[a]	JMG14[c]	JMG17[c]	2JMG28[c]	JMG4[d]	JMG6[d]	JMG8[a]	JMG9[d]	JMG10[d]
Lat. (°N)	24°25′	24°16′	24°12′	24°25′	24°20′	24°15′	24°16′	24°18′	24°19′	24°14′
	18.7″	57.0″	11.0″	07.7″	30.0″	29.7″	34.6″	00.2″	16.8″	20.7″
Long. (°E)	73°45′	73°50′	73°58′	73°45′	73°48′	73°52′	73°50′	73°49′	73°49′	73°56′
	41.7″	24.4″	49.2″	35.2″	04.1″	23.8″	42.7″	22.1″	02.5″	19.6″
SiO_2 (wt%)	67.3	66.8	68.7	69.1	70.0	74.7	75.4	75.3	76.7	76.3
TiO_2	0.41	0.50	0.46	0.35	0.34	0.15	0.09	0.12	0.09	0.08
Al_2O_3	15.52	15.50	15.53	15.82	14.40	14.45	14.03	14.06	12.63	14.22
$Fe_2O_3^t$	3.35	3.95	3.31	2.99	2.58	1.22	0.89	1.34	1.14	0.72
MnO	0.02	0.03	0.04	0.03	0.03	0.01	0.01	0.02	0.02	0.01
MgO	1.51	1.77	1.08	1.25	1.08	0.74	0.47	0.51	0.48	0.23
CaO	1.36	2.31	3.09	1.02	1.38	0.54	0.61	1.71	0.92	1.55
Na_2O	6.65	4.65	4.10	4.48	4.28	6.95	6.30	5.18	3.55	4.70
K_2O	1.37	2.45	3.31	3.50	3.27	1.26	1.51	1.35	4.40	1.62
P_2O_5	0.14	0.20	0.17	0.13	0.12	0.04	0.02	0.03	0.05	0.02
LOI	1.18	0.89	0.78	1.74	1.62	0.65	0.64	0.84	0.76	0.99
Sum	98.8	99.1	100.6	100.3	99.1	100.7	100.0	100.5	100.7	100.4
Sc (ppm)	3	7	5	4	2	2	2	2	2	2
V	49	60	49	38	32	16	7	12	11	< 5
Cr	< 20	30	< 20	< 20	< 20	< 20	< 20	20	< 20	< 20
Ni	< 20	< 20	< 20	< 20	< 20	< 20	< 20	< 20	< 20	< 20
Zn	< 30	< 30	50	< 30	40	< 30	< 30	< 30	< 30	< 30
Ga	18	19	19	19	16	14	13	14	14	14
Rb	45	73	79	95	66	22	28	41	87	24
Sr	196	356	472	160	213	93	125	257	208	264
Y	10	14	11	8	7	9	11	17	12	4
Zr	163	141	149	144	143	88	65	69	76	68
Nb	4	3	7	11	2	7	5	6	3	3

Table 2 (continued)

Rock type	TTGs		Transitional TTGs			Altered granitoids				
Sample no.	2JMG25[a]	2JMG27[a]	JMG14[c]	JMG17[c]	2JMG28[c]	JMG4[d]	JMG6[d]	JMG8[a]	JMG9[d]	JMG10[d]
Ba	320	541	782	619	1217	240	313	205	927	587
Pb	< 5	9	12	< 5	9	< 5	< 5	8	24	16
Th	8.5	5.8	6.6	5.5	4.7	10.6	5.4	4.9	11.7	2.2
U	1.8	1.8	0.9	3.3	0.7	1.1	1	1.4	1.9	0.6
Hf	3.1	3.1	3.7	3.5	3.1	2.2	1.8	1.9	2.2	1.9
Ta	0.5	0.7	0.6	1	0.4	0.5	0.4	0.6	0.3	0.2
La	39.4	36.4	34.6	41.2	29.7	24.5	11.8	12	18	9
Ce	72.9	71.3	62.5	77.1	53	45.8	21.9	23.3	34.1	15.1
Pr	7.54	7.94	7.03	8.17	5.56	4.86	2.32	2.57	3.88	1.61
Nd	27.3	29.3	26.2	28.4	19.3	17.9	8.5	9.3	14.6	5.7
Sm	4.5	5.1	4.4	4.7	3	3.2	1.6	2	3.1	1.2
Eu	1.18	1.18	1.02	1.01	0.81	0.54	0.44	0.58	0.68	0.58
Gd	3.4	3.4	3	3	1.8	2	1.4	1.8	2.5	0.9
Tb	0.4	0.5	0.4	0.4	0.3	0.3	0.3	0.3	0.4	0.1
Dy	2.4	2.7	2.4	2	1.3	1.6	1.7	2.3	2.2	0.7
Ho	0.4	0.5	0.4	0.3	0.2	0.3	0.4	0.6	0.4	0.1
Er	1	1.4	1.2	1	0.6	0.9	1.2	1.9	1.1	0.3
Tm	0.13	0.2	0.17	0.19	0.08	0.13	0.19	0.32	0.15	< 0.05
Yb	0.8	1.3	1	1.4	0.5	0.8	1.2	2.2	0.9	0.3
Lu	0.13	0.18	0.15	0.21	0.07	0.14	0.2	0.35	0.15	0.06
∑ REE	161.5	161.4	144.5	169.1	116.2	103.0	53.2	59.5	82.2	37.5
$(Gd/Er)_N$	2.7	2.0	2.0	2.4	2.4	1.8	0.9	0.8	1.8	2.4
$(La/Yb)_N$	35.2	20.0	24.7	21.0	42.5	21.9	7.0	3.9	14.3	21.4
$(Gd/Yb)_N$	3.5	2.1	2.4	1.7	2.9	2.0	1.0	0.7	2.3	2.4
Eu/Eu*	0.91	0.86	0.85	0.81	1.06	0.65	0.89	0.93	0.74	1.69
Na_2O/K_2O	4.86	1.90	1.24	1.28	1.31	5.52	4.17	3.58	0.18	2.90
K_2O/Na_2O	0.21	0.53	0.81	0.78	0.76	0.18	0.24	0.26	1.24	0.34
Mg#	47	47	39	45	45	54	51	43	45	39
FM oxides	4.89	5.71	4.56	4.32	3.68	1.99	1.37	1.85	1.62	0.97
$FeO^T + MgO$	4.53	5.33	4.06	3.94	3.40	1.84	1.27	1.72	1.51	0.88
Ba + Sr	516	897	1254	779	1430	333	438	462	1135	851
La/Sm	8.76	7.14	7.86	8.77	9.90	–	–	–	–	–
Nb/Sm	0.89	0.59	1.59	2.34	0.67	–	–	–	–	–
U/Th	0.21	0.31	0.14	0.60	0.15	–	–	–	–	–
Th/Yb	10.63	4.46	6.60	3.93	9.40	–	–	–	–	–
Ba/La	8.12	14.86	22.60	15.02	40.98	–	–	–	–	–
Nb/Nb*	0.05	0.05	0.11	0.17	0.04	–	–	–	–	–
Pb/Pb*	–	3.97	6.00	–	5.50	–	–	–	–	–
ASI	1.07	1.10	1.00	1.25	1.12	1.06	1.07	1.08	1.04	1.16

[a]Tonalite [b]Quartz diorite [c]Granodiorite [d]Alkali feldspar granite; N: Chondrite normalized; $Eu/Eu^* = Eu_N/(Sm_N \times Gd_N)^{½}$; Mg#: $100 \times Mg^{2+}/(Mg^{2+} + Fe_t)$; FM oxides: Ferromagnesian oxides = $(FeO^t + MgO + MnO + TiO_2)$ wt%; $Nb/Nb^* = Nb_N/(Th_N \times La_N)^{½}$; $Pb/Pb^* = Pb_N/(Ce_N \times Pr_N)^{½}$, where N = N-MORB normalized value after Sun and McDonough (1989). *ASI* aluminum saturation index = molar $Al_2O_3/(CaO - 3.3P_2O_5 + Na_2O + K_2O)$

$Er)_N$ = 1.6–2.7, V (28–60 ppm), and Cr (< 20–40 ppm) abundances, and overall moderate to high LREE [$(La/Yb)_N$ = 15.7–35.2] contents. The high Na_2O abundances along with relatively low K_2O/Na_2O ratios, low Ba + Sr, $(Gd/Er)_N$, and ferromagnesian oxides in these rocks are similar to those of Archean TTGs (Martin et al. 2005; Halla et al. 2009; Moyen and Martin 2012; Laurent et al. 2014). In addition, the geochemical classification diagrams distinctly

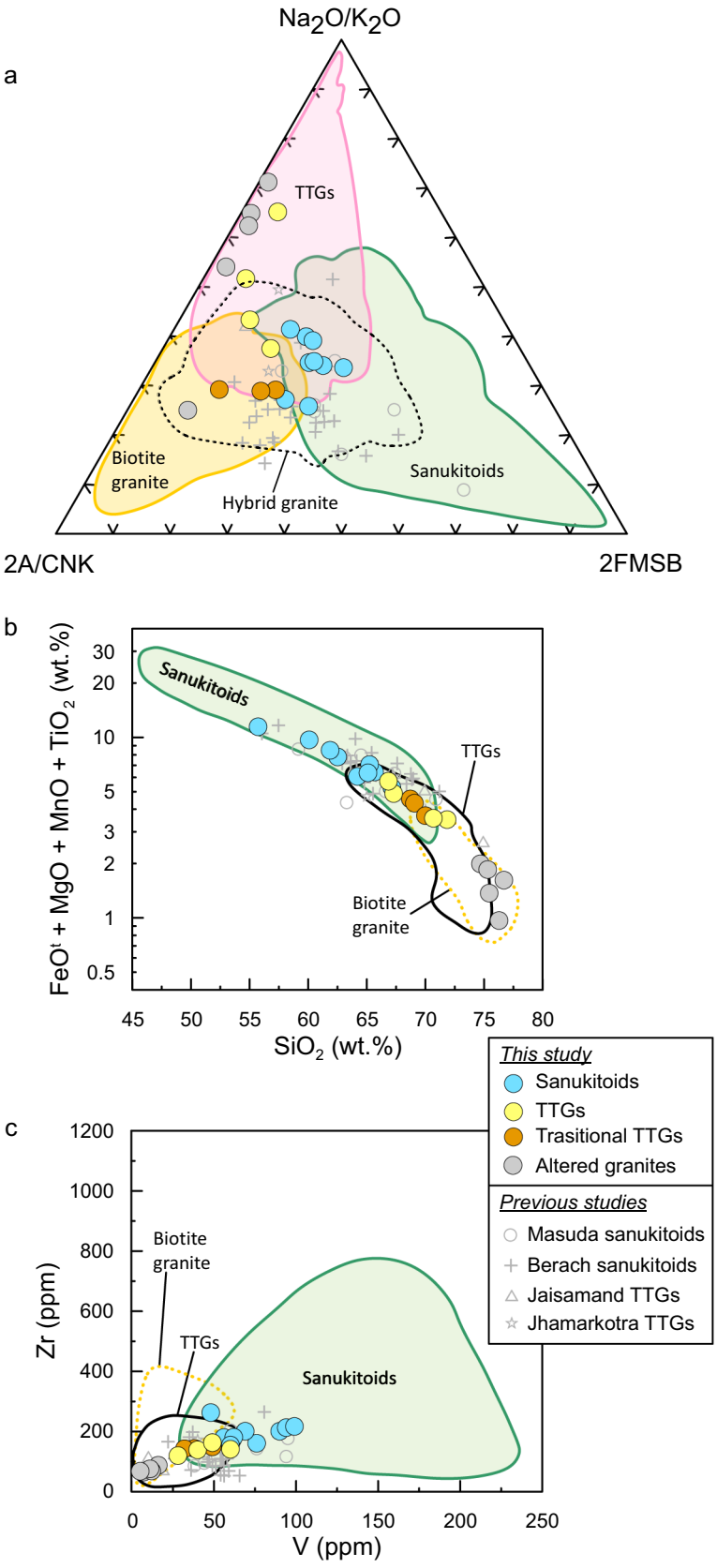

Fig. 7 **a** Ternary Na_2O/K_2O–2A/CNK–2FMSB; **b** binary SiO_2 (wt%) versus $FeO^t + MgO + MnO + TiO_2$ (wt%) and **c** binary V (ppm) versus Zr (ppm) plots (Laurent et al. 2014). Data used for previous studies: Masuda sanukitoids = Kaur et al. (2023a); Berach sanukitoids = Mondal and Raza (2013), Rahaman and Mondal (2015) and Kaur et al. (2019a); Jaisamand TTGs = Rahaman and Mondal (2015) and Jhamarkotra TTGs = Kaur et al. (2019a)

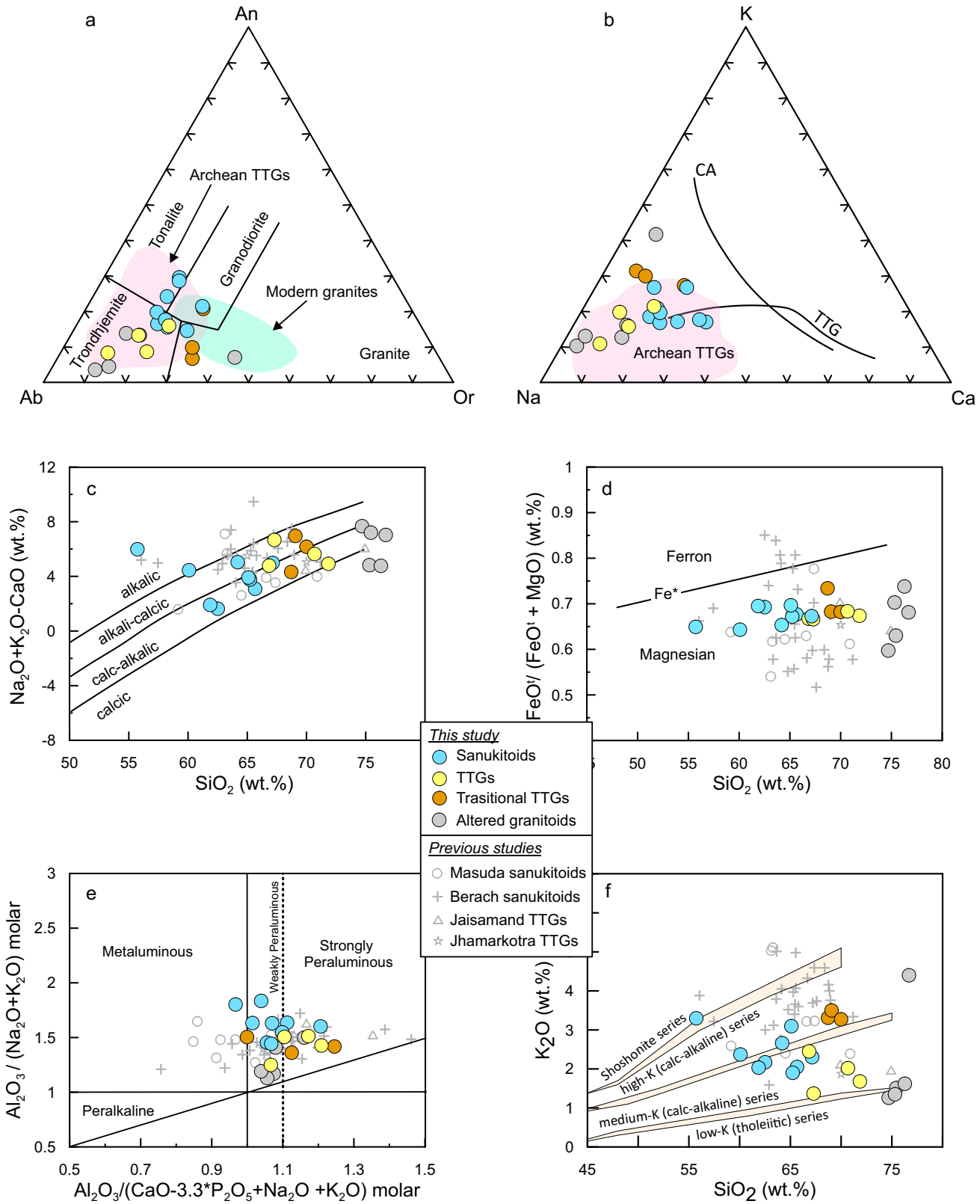

Fig. 8 Geochemical classification and characterization of the Jaisamand granitoids in **a** normative An–Ab–Or diagram (Barker 1979) with the fields of Archean TTGs and modern granites after Moyen and Martin (2012); **b** cationic K–Na–Ca diagram (Barker and Arth 1976) with the field of Archean TTGs after Moyen and Martin (2012); **c** modified alkali–lime index $Na_2O + K_2O - CaO$ (wt%) versus SiO_2 (wt%) diagram (Frost et al. 2001); **d** $FeO^t/(FeO^t + MgO)$ (wt%) versus SiO_2 (wt%) diagram (Frost et al. 2001; Frost and Frost 2008); **e** Shand aluminum saturation index (ASI) plot (Maniar and Piccoli 1989; Bucholz and Spencer 2019), and **f** K_2O (wt%) versus SiO_2 (wt%) diagram (Rickwood 1989). Data for previous studies are the same as in Fig. 7. *CA* calc-alkaline, *TTG* trondhjemite trends

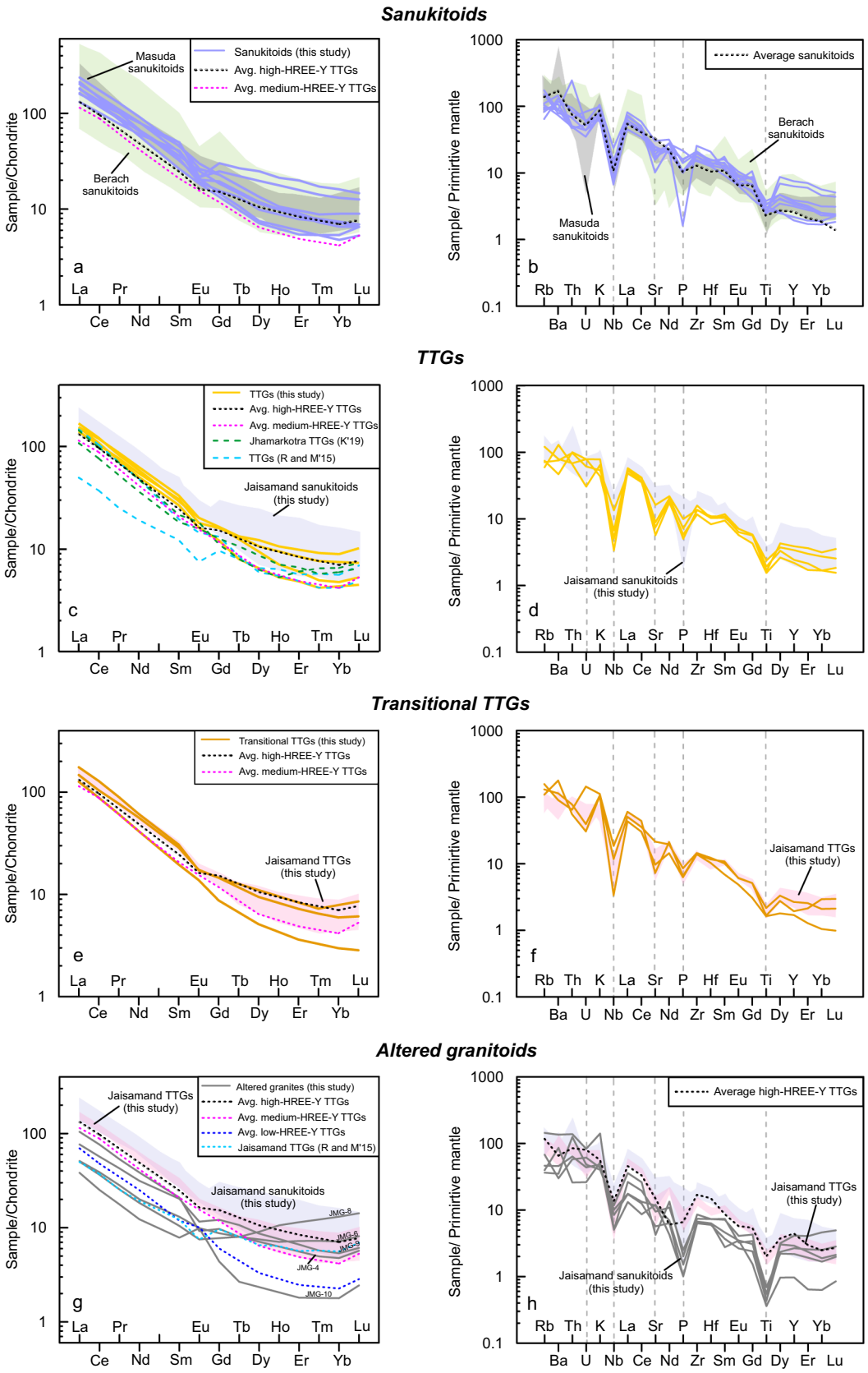
Sanukitoids
Sanukitoids (this study)
Avg. high-HREE-Y TTGs
Avg. medium-HREE-Y TTGs
Masuda sanukitoids
Berach sanukitoids
Sample/Chondrite
a
La Pr Eu Tb Ho Tm Lu
Ce Nd Sm Gd Dy Er Yb
Average sanukitoids
Sample/ Primitive mantle
b
Rb Th K La Sr P Hf Eu Ti Y Yb
Ba U Nb Ce Nd Zr Sm Gd Dy Er Lu
TTGs
TTGs (this study)
Avg. high-HREE-Y TTGs
Avg. medium-HREE-Y TTGs
Jhamarkotra TTGs (K'19)
TTGs (R and M'15)
Jaisamand sanukitoids (this study)
c
d
Transitional TTGs
Transitional TTGs (this study)
Avg. high-HREE-Y TTGs
Avg. medium-HREE-Y TTGs
Jaisamand TTGs (this study)
e
f
Altered granitoids
Altered granites (this study)
Avg. high-HREE-Y TTGs
Avg. medium-HREE-Y TTGs
Avg. low-HREE-Y TTGs
Jaisamand TTGs (R and M'15)
JMG-8
JMG-6
JMG-9
JMG-4
JMG-10
g
Average high-HREE-Y TTGs
h

◂**Fig. 9** Chondrite-normalized REE and primitive mantle-normalized multi-element patterns for the sanukitoids (**a**, **b**), TTGs (**c**, **d**), transitional TTGs (**e**, **f**), and altered granitoids (**g**, **h**). The normalizing values for Chondrite are after Barrat et al. (2012) and those of primitive mantle are after Palme and O'Neill (2014). Data source: average high-HREE-Y TTGs, medium-HREE-Y TTGs and low-HREE-Y TTGs: Moyen and Martin (2012), average sanukitoids: Halla et al. (2009), Masuda and Berach sanukitoids: same as in Fig. 7; Jhamarkotra TTGs (K'19): Kaur et al. (2019a) and Jaisamand TTGs (R and M'14): Rahaman and Mondal (2015)

indicate TTG affinity of these rocks and also distinguish them from the sanukitoids (Fig. 7a–c).

In the normative An–Ab–Or and cationic K–Na–Ca diagrams, the analyzed samples occupy the field of Archean TTGs (Fig. 8a, b), confirming their TTG affinity. The Jaisamand TTGs are largely calc-alkalic to alkali-calcic, magnesian, weakly peraluminous to strongly peraluminous (ASI = 1.07–1.21; Table 2), and of medium-K (calc-alkaline) affinity (Fig. 8c–f).

In the chondrite-normalized REE diagram, the TTGs show moderate to highly fractionated REE patterns [$(La/Yb)_N$ = 15.7–35.2] with slight to negligible Eu anomalies (Eu/Eu* = 0.81–0.91) and flat to depleted HREE profiles [$(Gd/Yb)_N$ = 1.8–3.5] (Fig. 9c; Table 2). The overall REE patterns are comparable with either high-HREE-Y TTGs or medium-HREE-Y TTGs, and also with previously studied adjoining Jhamarkotra TTGs (Kaur et al. 2019a), Jaisamand TTGs (one sample; Rahaman and Mondal 2015), and Jaisamand sanukitoids (this study). In the primitive mantle-normalized multi-element diagram, the TTGs show negative Nb, Sr, P, and Ti anomalies, and the patterns are comparable with those of the Jaisamand sanukitoids (Fig. 9d).

4.2.3 Transitional TTGs

In comparison to the TTGs (Table 2), these rocks show lower Na_2O (4.10–4.48 wt%) and Na_2O/K_2O ratios (1.24–1.31), Mg# (39–45) and higher K (K_2O = 3.27–3.50 wt%) and K_2O/Na_2O (0.76–0.81) ratios, but overlapping ranges for Si (SiO_2 = 68.7–70.0 wt%), Al (Al_2O_3 = 14.40–15.82 wt%), Ca (CaO = 1.02–3.09 wt%), Mg (MgO = 1.08–1.25 wt%), Fe ($Fe_2O_3^t$ = 2.58–3.31 wt%), and FM oxides (3.68–4.56) and $(Gd/Er)_N$ = 2.0–2.4. These overlapping geochemical characteristics with the TTGs and higher K (K_2O = 3.27–3.50 wt%) abundances than TTGs but overlapping Ba + Sr (779–1430 ppm) and lower FM oxides and Mg (MgO = 1.08–1.25 wt%) content than the sanukitoids, indicate transitional TTG affinity for these rocks (Champion and Smithies 2001, 2003, 2019; Laurent et al. 2014; Joshi et al. 2017). In the geochemical discrimination diagrams, these rocks fall in both the TTGs and the sanukitoids fields, supporting their transitional nature (Fig. 7a–c).

The transitional TTGs mostly lie at the outer margins for the field of Archean TTGs in the normative An–Ab–Or and cationic K–Na–Ca diagrams (Fig. 8a, b). The rocks are calc-alkalic to alkali-calcic, magnesian, weakly peraluminous to strongly peraluminous (ASI = 1.00–1.25; Table 2), and belong to the high-K (calc-alkaline) series (Fig. 8c–f).

In the chondrite-normalized REE diagram, the transitional TTGs show moderate to strong REE fractionation [$(La/Yb)_N$ = 21.0–42.5] with flat to slightly depleted HREE profiles [$(Gd/Yb)_N$ = 1.7–2.9] and small negative to no Eu anomalies (Eu/Eu* = 0.81–1.06; Fig. 9e; Table 2). The overall REE patterns of two samples are comparable with the average high-HREE-Y TTGs, while one sample (2JMG28) can be compared with medium-HREE TTGs. Further, the REE patterns of the transitional TTGs overlap with those of Jaisamand TTGs (except sample 2JMG28; Fig. 9e). In the primitive mantle-normalized multi-element diagram, the transitional TTGs show negative Nb, Sr, P, and Ti anomalies, like those observed in the Jaisamand TTGs (Fig. 9f).

4.2.4 Altered granitoids

These granitoids are characterized by very high Si abundances (SiO_2 = 74.7–76.7 wt%) and a disparity in alkalis, as, in some samples where K-feldspar occurs as an accessory relict phase, the Na_2O (6.30–6.95 wt%) contents are much higher than those of K_2O (1.26–1.51 wt%; Table 2). This is a typical feature of primary granitoids undergoing albitization during an alkali ion exchange fluid-induced mechanism (e.g., Moore and Liou 1979; Kaur et al. 2012, 2019b). Moreover, the lower abundances of ferromagnesian oxides (0.97–1.99 wt%) also indicate dissolution of mafic phases during alteration, which is also supported by the lower amounts of biotite in these rocks (Tables 1, 2). These rocks also show lowest ΣREE (37.5–103.0 ppm) among all the other granitoid types, and REE depletion is a common feature during metasomatism of granitoids (Boulvais et al. 2007; Kaur et al. 2012). Considering the above, the altered granitoids are not suitable to characterize in various classification and discrimination diagrams as they are likely to provide misleading information (Kaur et al. 2014). Therefore, these granitoids are not discussed in such diagrams, although their plots are shown.

In the chondrite-normalized REE diagram, the altered granitoids can be distinguished into two groups: (1) low fractionated REE group [$(La/Yb)_N$ = 3.9–7.0; samples JMG6 and JMG8] with flat HREE patterns [$(Gd/Yb)_N$ = 1.0–0.7] and very small negative Eu anomalies (Eu/Eu* = 0.89–0.93), and (2) moderately fractionated REE group [$(La/Yb)_N$ = 14.3–21.9; samples JMG4, JMG9 and JMG10] with slightly depleted HREE patterns [$(Gd/Yb)_N$ = 2.0–2.4] and negative to positive Eu anomalies (Eu/Eu* = 0.65–1.69; Fig. 9g; Table 2). The overall pattens are depleted in REE, particularly in LREE compared with the

patterns of average high-HREE-Y TTGs, medium-HREE-Y TTGs, and the Jaisamand sanukitoids and TTGs (this study); however, the REE patterns show similarity with a previously published sample of Jaisamand TTGs (Rahaman and Mondal 2015; Fig. 9g). In the primitive mantle-normalized multi-element diagram, the altered granitoids show negative Nb, P, and Ti anomalies and mostly lower values for LILE, LREE, and HFSE compared to the average high-HREE-Y TTGs, and to the Jaisamand sanukitoids and TTGs (Fig. 9h).

5 Discussion

5.1 Consequences of metasomatic alteration

The Archean granitoids are commonly subjected to multiple phases of deformation and metamorphism. Therefore, it is important to evaluate the effects of post-crystallization events on these rocks. As shown in the "Results" section, a few samples of the Jaisamand granitoids exhibit effects of Na-metasomatism or albitization, and these samples have been excluded from discussion related to granitoid characterization to avoid misleading interpretations.

In this context, the compositional changes in feldspars, particularly in plagioclase, are significant. The contents of Na, K, Ca, and Si are prone to alteration during varying degrees of feldspar albitization. The transformation of K-feldspar to albite is driven by an alkali-ion exchange mechanism between a Na-rich fluid and feldspar phases (Orville 1963; Moore and Liou 1979; Kaur et al. 2012). The deanorthization of oligoclase, that is, the metasomatic alteration of oligoclase to albite, involves the fluid-mediated infiltration of Na^+ and Si^{4+} with the simultaneous removal of Ca^{2+} and Al^{3+} (Engvik et al. 2008; Plümper and Putnis 2009). The plagioclase compositions of the Jaisamand altered granitoids reflect the deanorthization of oligoclase. For example, sample JMG8 shows plagioclase composition varying between $An_{6.8}$ and $An_{16.2}$ (Table S1), while the plagioclase in other altered granitoids is predominantly pure albite. Such transformation of feldspars to virtually pure albite further affects the whole-rock geochemistry, resulting in significant gains in Na (albitization) and Si (silicification) and losses in K and Ca (Table 2). For instance, the effects of albitization can be observed in Fig. 7a, where these rocks exhibit higher Na_2O/K_2O ratios, while silicification is evident in Figs. 7b, 8c, d, as these rocks form a separate cluster with the highest Si values.

Most importantly, the occurrence of plagioclase with An contents ≤ 5 classifies these rocks as alkali–feldspar granite, according to IUGS recommendations (Streckeisen 1976). Furthermore, the dissolution of mafic phases not only alters the Fe and Mg contents but also results in a loss of REE. The loss of ferromagnesian elements and the enrichment in Na pose a challenge in determining whether the rocks were originally TTGs, sanukitoids, or potassic granites. The significant REE loss during albitization must also be carefully considered, as the altered Jaisamand granitoids with the lowest REE contents may give the misleading impression that some of these rocks have a low-HREE-Y affinity (Fig. 9g). Therefore, determination of plagioclase compositions along with a careful examination of petrographic evidence of metasomatism in the Archean granitoids is critical to avoid misclassification and misinterpretations.

5.2 Petrogenesis

Megascopically, the Jaisamand TTGs, sanukitoids, and transitional TTGs show similar textural characteristics, making it difficult to distinguish between them in the field. Additionally, the absence of cross-cutting relationships among these granitoids suggests their nearly coeval emplacement. Furthermore, coeval Neoarchean TTGs and sanukitoids (2560–2540 Ma) have also been reported from the Aravalli–BGC (Kaur et al. 2023a). The Archean lineage of the Jaisamand granitoids is reflected by various classification and discrimination diagrams (Figs. 8a, b, 11c), which show no post-Archean affinity. This is further corroborated by the occurrence of sanukitoids, most of which appeared during the Neoarchean (e.g. Laurent et al. 2011; Mikkola et al. 2014; Jiang et al. 2016; Smithies et al. 2019; Bruno et al. 2020; Jayananda et al. 2020; Singh et al. 2021; Kaur et al. 2023a). Therefore, it is reasonable to conclude that the different granitoid types within the Jaisamand pluton were emplaced nearly synchronous during the Neoarchean. Their overlapping REE and multi-element patterns (Fig. 9c–f) also indicate a genetic relationship between them.

5.2.1 TTGs

The most widely accepted process for the formation of Archean TTGs is the anatexis of hydrated metabasite at varying depths of 35–70 km or pressures between 1 and 2 GPa (Jahn et al. 1981; Rapp et al. 1991, 2003; Foley et al. 2002; Moyen 2011; Moyen and Martin 2012; Nagel et al. 2012; Laurent et al. 2014, 2024; Johnson et al. 2017; Kendrick et al. 2024). The Jaisamand TTGs are Si-rich ($SiO_2 > 65\%$) with lower MgO and Mg# and low contents of transition elements (V, Sc, Cr, and Ni), indicating that these TTG melts were derived from a crustal source (Table 2). This is also supported by high $(La/Sm)_N$ ratios (4.6–5.7) and low Nb/La (0.06–0.24) and Nb/Ce (0.03–0.13) ratios of the TTGs, relative to the average ratios in the mantle [$(La/Sm)_N = 1.0$, Nb/La = 1.02 and Nb/Ce = 0.40; McDonough and Sun 1995). Moreover, the Hf isotope signatures (εHf_t values = − 8.6 to − 2.0 and two-stage Hf model ages: T_{DM2} = 3.4–3.2 Ga) of the Jhamarkotra Neoarchean TTGs (2.56–2.55 Ga;

15–20 km north of the Jaisamand pluton; Fig. 2; Kaur et al. 2019a) also indicate their derivation from the melting of older Paleoarchean crust.

In the ternary source discrimination diagram of Laurent et al. (2014), the Jaisamand and Jhamarkotra TTGs plot in the low-K to high-K mafic rock fields, indicating a predominantly mafic nature of the crustal source (Fig. 10a). Also, the TTGs occupy the fields of experimental melts derived from amphibolite or metabasalt in the discrimination diagrams (Fig. 10b–e), consistent with metabasite source(s). The relatively low Cr and moderate Mg# are also comparable to the TTG melts derived from a lower crustal mafic source (Fig. 11a), suggesting limited interaction of these TTGs melts with the mantle wedge peridotite. This is in good agreement with their peraluminous affinity and relatively low $FeO^t + MgO$ (< 10 wt%) and Ba + Sr contents (Fig. 11b). The "sub-types" of TTGs, the "high-pressure", "low-pressure", and "medium pressure" groups, can be identified on the basis of their HREE, Sr, and Nb–Ta contents. The high-pressure group TTGs are characterized by low HREE, low Nb–Ta, and high Sr, indicating the presence of significant garnet and some rutile, but no plagioclase in the residue. In contrast, the low-pressure group TTGs display high- HREE, Nb, and Ta but lower Sr, suggesting the presence of plagioclase in the residue, with less garnet and no rutile. The medium-pressure group falls between these two groups. The stabilities of plagioclase, garnet, and rutile are strongly pressure-dependent, that is, pressure conditions significantly influence partial melting reactions, which in turn affect REE concentrations. Therefore, REE patterns can provide information about the depth of melting (López et al. 2006; Halla et al. 2009; Moyen 2011).

The Jaisamand TTGs (except the sample 2JMG23) show relatively high HREE ($\sum$HREE = 8.7–11.2 ppm), Nb (3–8 ppm), Ta (0.5–0.8 ppm), and low Sr (165–356 ppm), classifying them as a low-pressure group, suggesting that they formed at shallow depths (≤ 1.0 GPa) with plagioclase in the residue and less or insignificant garnet and no rutile. This is also supported by their REE patterns, which show an affinity with the high-HREE-Y TTG group (Fig. 9c), showing nearly flat to slightly inclined HREE-profiles [$(Gd/Yb)_N$ = 1.8–3.5] and slightly negative Eu anomalies. Sample 2JMG23, however, has relatively low HREE ($\sum$HREE = 6.8 ppm), Nb (2 ppm), Ta (0.4 ppm), and Sr (125 ppm) compared to other Jaisamand TTGs, and exhibits an REE pattern similar to the medium-HREE-Y TTG group TTG (Fig. 9c). This suggests that it formed at relatively high pressure, where plagioclase and relatively more garnet were present in the residue. The modal proportion of residual garnet increases as a function of pressure, ranging from < 5% at 1.0 GPa up to 90% at 2.5 GPa (Moyen and Martin 2012). Therefore, the Jaisamand TTGs were generated at shallow to moderate depths (1.0–1.2 GPa), above the garnet-in line but still within the plagioclase stability field (Rapp et al. 1999; Moyen 2011; Laurent et al. 2024). Furthermore, the relatively high $(La/Yb)_N$ ratios (15.7–35.2) and low $(Yb)_N$ abundances (4.76–8.93), which are consistent with Archean TTGs, can be attributed to variable amount of garnet in the residue (Fig. 11c).

The geochemical variations in the TTGs may be attributed to varying extent of fractional crystallization or partial melting. Nearly constant values of Eu anomalies (Eu/Eu* = 0.81–0.91) with increasing Sr contents (Fig. 11d) rule out significant plagioclase fractionation. The pair of elements with high (C^H) and moderate incompatibility (C^M) can discriminate the processes of magma generation (Schiano et al. 2010 and references therein). On the La versus La/Sm and Nb versus Nb/Sm incompatible element pair plots, the TTGs do not follow a horizontal trend of fractional crystallization, indicating partial melting to be the dominant process of magma generation (Fig. 11e, f).

5.2.2 Sanukitoids

The emplacement of sanukitoids during the Archean–Paleoproterozoic transition marks the beginning of Wilson-style plate interactions, producing high-K calc-alkaline granitoids (Shirey and Hanson 1984; Heilimo et al. 2010; Martin et al. 2009; Laurent et al. 2014; Moyen and Laurent 2018). The experimental and geochemical results suggest that the generation of sanukitoid melts can be through either a single-stage or a two-stage process, both of which require interaction between mantle peridotite and a crustal component, such as TTG melts or sediment-derived melts or both (Moyen et al. 2001, 2003; Halla 2005; Martin et al. 2009; Heilimo et al. 2010; Rapp et al. 2010; Oliveira et al. 2011; Almeida et al. 2013).

The relatively high Si (SiO_2 = 55.7–67.1 wt%), MgO (MgO = 1.54–3.76 wt%), transition metal content (V = 48–99 ppm and Cr = 20–90 ppm), and incompatible elements (Ba + Sr = 823–1407 ppm; Table 2) in the Jaisamand sanukitoids indicate interaction of TTG melts with mantle wedge peridotite (Smithies 2000; Martin and Moyen 2002; Martin et al. 2005). The diversity in chemical composition of sanukitoids is either related to interactions between peridotite and incompatible element-rich components at mantle levels, primarily a TTG melt (Martin et al. 2009; Heilimo et al. 2010; Laurent et al. 2014), or to the differentiation of mafic magmas by amphibole and plagioclase fractionation (Stern and Hanson 1991; Laurent et al. 2013). The latter possibility can be ruled out, as the Jaisamand sanukitoids do not follow the horizontal trend of fractional crystallization (Fig. 11e, f) in the high (C^H) and moderate incompatible (C^M) element pair diagrams. The lack of correlation between Eu/Eu* and Sr abundances (Fig. 11d) also suggests that plagioclase fractionation played

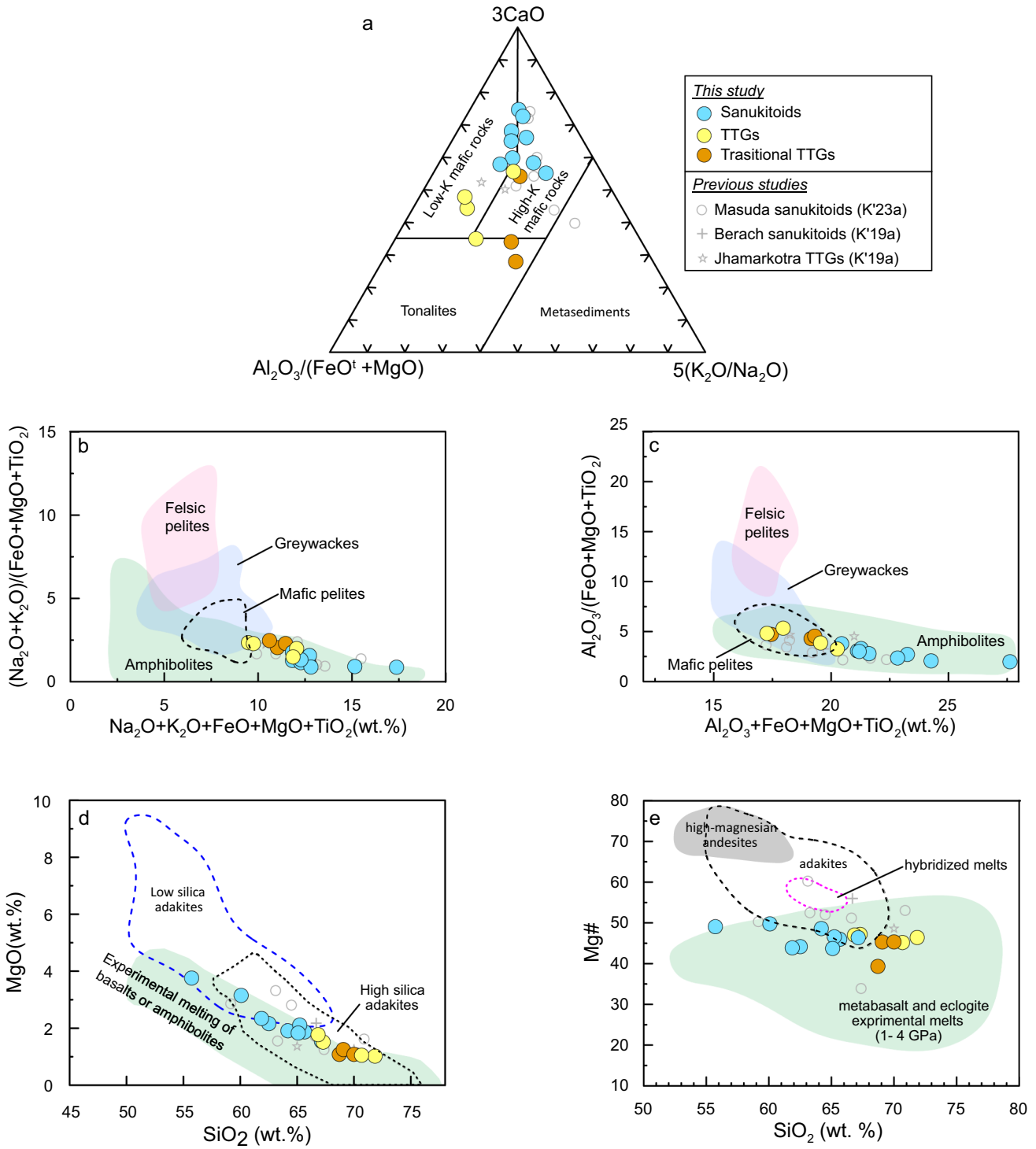

Fig. 10 Source discrimination diagram for the Jaisamand granitoids: **a** ternary 2CaO − Al_2O_3/(FeO^t + MgO) − 5(K_2O/Na_2O) plot (Laurent et al. 2014); **b** Na_2O + K_2O + FeO + MgO + TiO_2 (wt%) versus (Na_2O + K_2O)/(FeO + MgO + TiO_2) and **c** Al_2O_3 + FeO + MgO + TiO_2 (wt%) versus Al_2O_3/(FeO + MgO + TiO_2), along with the fields for composition of melts produced by experimental dehydration melting of amphibolites, mafic pelites, graywacke, and felsic pelites (Patiño Douce 1999); **d** SiO_2 (wt%) versus MgO (wt%) plot along with fields of low-silica adakites, high-silica adakites, and experimental melting of basalts and amphibolites (Martin et al. 2005) and **e** SiO_2 (wt%) versus Mg# plot along with fields for pristine experimental melts generated by metabasalt and eclogite, high-magnesian andesites, adakites, and hybridized melts (Stern and Kilian 1996; Rapp et al. 1999; Smithies 2000; Sisson et al. 2005). Previous studied samples: Masuda sanukitoids (K'23a): Kaur et al. 2023a, Berach Sanukitoid and Jhamarkotra TTGs (K'19a): Kaur et al. (2019a)

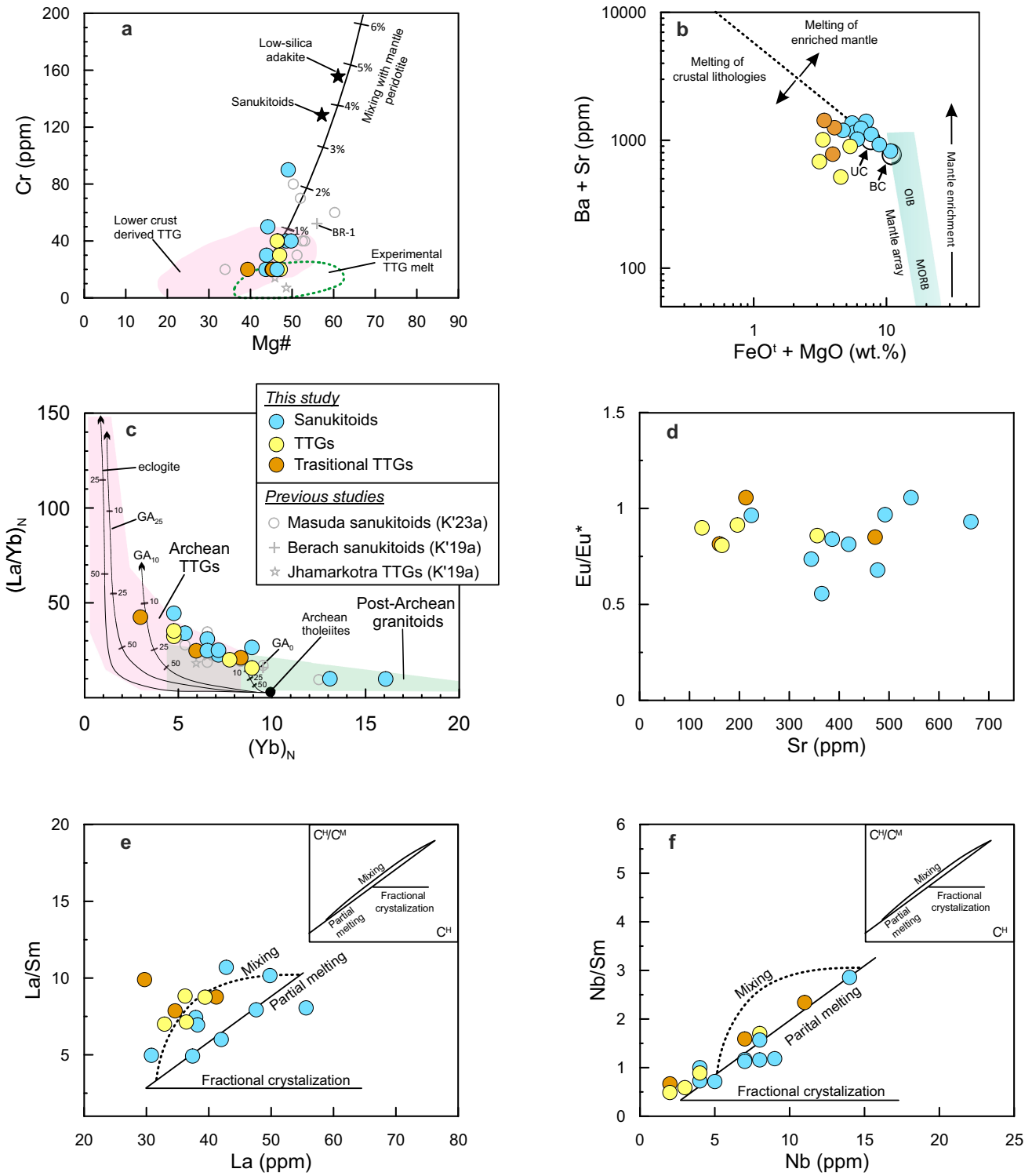

Fig. 11 Bivariant diagram related to source characteristics of the Jaisamand granitoids: **a** Mg# versus Cr (ppm) (Qian and Hermann 2013); **b** FeO^t + MgO (wt%) versus Ba + Sr (ppm) along with bulk continental (*BC*) and upper continental composition fields (*UC*) (Laurent et al. 2014); **c** $(Yb)_N$ versus $(La/Yb)_N$ plot along with evolutionary trends for the partial melting of Archean tholeiites with residual minerology of eclogite, garnet-free amphibolite, and amphibolites with 25% and 10% garnet (GA_{25} and GA_{10}) (Martin 1986); **d** Sr (ppm) versus (Eu/Eu*) plot; **e** La (ppm) versus (La/Sm), and **f** Nb (ppm) versus (Nb/Sm) plots (Schiano et al. 2010). Previously studied samples are the same as in Fig. 10

an insignificant role, indicating a predominant influence of partial melting. Like TTGs, the sanukitoids were derived from low-K to high-K mafic sources (Fig. 10a). The mafic source for the sanukitoids is also supported by several discrimination diagrams based on the experimental results of different melt compositions (Fig. 10b–e).

Based on their TiO_2 and MgO contents, the sanukitoids can be classified into low-Ti and high-Ti types, which have genetic implications for the origin of these rocks (Martin et al. 2009 and references therein). The Jaisamand sanukitoids are classified as the low-Ti-type (Fig. 12a), which formed through interaction between TTG melts (during their ascent) and overlying mantle wedge peridotite (i.e., a single stage process: Rapp et al. 1999; Prouteau et al. 2001; Martin et al. 2009), rather than by melting of previously metasomatized peridotite by slab melts, with or without the involvement of terrigenous sediments (e.g. Halla 2005; Wang et al. 2009; Laurent et al. 2011; Oliveira et al. 2011; Jiang et al. 2016; Wang et al. 2024). The geochemical variability during the interaction between TTG melts and peridotite is influenced by physical conditions, such as pressure, temperature, and relative volumes of peridotite and TTG melts (Martin et al. 2009; Rapp et al. 2010). The high and variable Si content (SiO_2 = 55.7–67.1 wt%) in the Jaisamand sanukitoids suggests a variably high effective TTG melt-to-peridotite ratio (Martin et al. 2009), indicating that these sanukitoids formed from interactions between high-TTG and low-peridotite melt fractions. Further evidence for limited interaction with the mantle wedge peridotite includes an overlap between the Jaisamand sanukitoids and the field of Archean TTGs (Fig. 12b), and the overlapping REE and multi-element patterns between the sanukitoids and TTGs (Fig. 9c). Such limited interactions likely resulted in the nearly analogous quartzo-feldspathic mineralogy (Table 1), which may explain the similar megascopic appearance of these rocks.

The predominance of crustal source rather than the enriched mantle is also consistent with their low FeO^t + MgO and moderately high Ba + Sr abundances

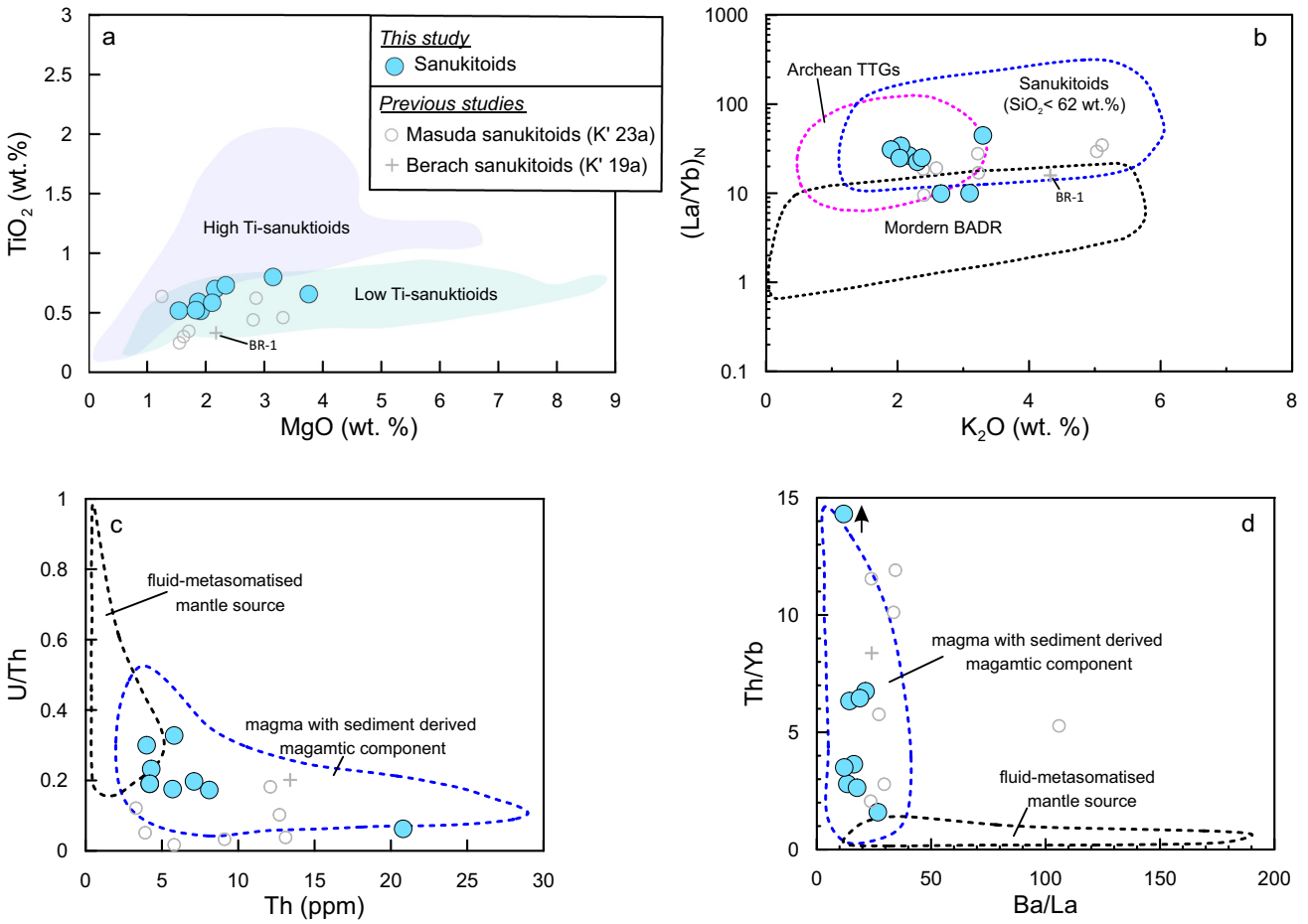

Fig. 12 **a** MgO (wt%) versus TiO_2 (wt%) with fields for low-Ti and high-Ti sanukitoids (Martin et al. 2009); **b** K_2O (wt%) versus $(La/Yb)_N$ (Martin et al. 2009); **c** Th (ppm) versus U/Th (Laurent et al. 2011), and **d** Ba/La versus Th/Yb (Laurent et al. 2011). Previous studied samples: Masuda sanukitoids (K'23a): Kaur et al. 2023a and Berach Sanukitoid (K'19a): Kaur et al. 2019a

(Fig. 11b), as the sanukitoids fall either in the field of crust-derived granitoids or close to the intracrustal differentiation trend. The wide range of Mg (MgO = 1.54–3.76 wt%) and Cr (Cr = 20–90 ppm) abundances may be attributed to differential interaction between the TTG melts and peridotite. Furthermore, the variably low U/Th and Ba/La, along with high Th/Yb ratios in the sanukitoids (Fig. 12c, d), point to varying contributions of subducted sediments during the partial melting of the subducted slab (Laurent et al. 2011).

The variable $(La/Yb)_N$ (9.9–44.5) ratios and $(Yb)_N$ (0.80–0.27) contents (Fig. 11c) along with differentially fractionated REE patterns (Fig. 9a, c), suggest that the sanukitoid magmas were generated at varying depths. Moreover, the REE patterns show affinity with the high-HREE-Y TTG and medium-HREE-Y TTG groups, indicating that the sanukitoids were formed by melting of the mafic crust at low to moderate pressures, respectively, and at relatively shallow depths with garnet-poor residuum. This is consistent with a pressure of at least 800 MPa, as inferred from the presence of magmatic epidote in the Jaisamand sanukitoids (Zen and Hammarstrom 1984). This is because the occurrence of magmatic epidote in the plutonic rocks of granodiorite or tonalite composition indicates a minimum pressure of crystallization between 600 and 800 MPa (Crawford and Hollister 1982; Naney 1983; Zen and Hammarstrom 1984; Schmidt and Thompson 1996). Moreover, prominent negative Nb and Ti anomalies in the multi-element diagram (Fig. 9b) suggest the retention of titanite or ilmenite or both in the residue.

5.2.3 Transitional TTGs

These rocks broadly overlap in composition with the TTGs in terms of major element oxides, except for their higher K_2O and K_2O/Na_2O ratios and lower Na_2O and Mg# (Table 2); they also display identical REE and multi-element patterns with those of the TTGs (Fig. 9e, f). Like TTGs, these geochemical characteristics suggest a crustal protolith (metabasite) for the transitional TTGs (Fig. 10). This is also supported by their lower Cr contents and moderate Mg# (Fig. 11a), which are comparable to those of lower crust-derived TTGs and experimental TTG melts. Moreover, this is in consonance with relatively low $FeO^t + MgO$ (< 10 wt%) abundances in the transitional TTGs, and they plot in the field of granitoids derived from melting of crustal lithologies (Fig. 11b).

Significant variations in La/Yb_N (21.0–44.5) ratios, Yb_N (2.98–8.33) contents (Fig. 11c), and the absent to moderate Eu anomalies (Eu/Eu* = 0.81–1.06), along with the similarity of REE patterns with both high-HREE-Y TTG and medium-HREE-Y TTG groups, a feature common to both Jaisamand TTGs and sanukitoids, suggest that the transitional TTGs were also derived from magmas generated at variable pressures (depths). These sources likely had varying amounts of residual garnet, that is, involvement of both garnet-poor (shallow depth) or garnet-rich (deeper depth) sources. Like sanukitoids, the occurrence of magmatic epidote in the transitional TTGs (granodioritic in composition) constrains the minimum pressure of 800 MPa (ca. 30 km depth) for the generation of their magmas. The lack of any horizontal trends in the pair of incompatible element discrimination diagrams (Fig. 11e, f) further suggest insignificant fractional crystallization during their magma evolution.

The K-enrichment in transitional TTGs could result from the direct partial melting of an enriched basaltic precursor, hydrothermal alteration of the basaltic source, or the influence of fractional crystallization with or without assimilation or magma mixing (Champion and Smithies 2007; Rollinson et al. 2024). However, the first process is unlikely because typical Archean basalts are not enriched in LILE and are, in fact, low-K tholeiites, which are the likely source for the true TTGs (Rollinson et al. 2024 and references therein). Moreover, hydrothermal alteration and silicification of basalt protolith cannot be accounted for the extent of K-enrichment in the basalts, particularly in the Neoarchean (Rollinson et al. 2024). Fractional crystallization can also be ruled out, as the geochemical attributes in the transitional TTGs are inconsistent with such a process (Fig. 11e, f). The probability of magma mixing or mingling is inconsistent with the lack of microgranular enclaves in the Jaisamand granitoids (Champion and Smithies 2007). Therefore, an additional component is required to explain the K-enrichment during the genesis of transitional TTGs.

Subducted sediment input during slab melting is another possibility, but this process cannot explain the coexistence of high-HREE-Y and medium-HREE-Y transitional TTGs, which were generated at different depths with or without the participation of garnet (Champion and Smithies 2007; Almeida et al. 2010). The involvement of a significant component of older continental crust appears to be the most viable mechanism for the generation of Jaisamand transitional TTGs, characterized by elevated K or LILE abundances (Champion and Smithies 2001, 2003, 2019). It is pertinent to note that the subchondritic εHft values (− 7.3 to − 1.9) and significantly older T_{DM2} (3.4–3.1 Ga) of the Neoarchean TTGs (2560–2550 Ma) and sanukitoids (2545–2540 Ma) from the southern and central Aravalli–BGC suggest that they are not juvenile but derived from the melting of older Paleo- to Mesoarchean crust (Kaur et al. 2019a, 2021, 2023a). Furthermore, the existence of ancient Archean felsic crust is also reflected in the presence of a few zircon xenocrysts (2800–2650 Ma) in the Aravalli–BGC Neoarchean TTGs and sanukitoids (Kaur et al. 2019a, 2021, 2023a). Considering the above arguments, it is proposed that the true TTG melts, generated by the partial melting of subducted metabasite precursors at different pressures with

variable relative roles of residual garnet and plagioclase, interacted with older TTGs at lower and middle crustal levels. The partial melting of older TTGs, which would have a granitic composition, would disproportionately contribute K and other LILE (Rollinson et al. 2024) to the slab-derived TTG melts, thereby generating the Jaisamand transitional TTGs.

5.3 Tectonic setting and geodynamic implications

In the Archean terranes around the world, the Neoarchean Era is marked by the abundant TTGs, followed by the potassic granites and sparse sanukitoids, representing final stabilization of cratons. There is a consensus that these latter granitoid types are of subduction-related origin (Laurent et al. 2014). Although sanukitoid emplacement typically post-dates the major phase of TTG magmatism (Halla et al. 2009; Heilimo et al. 2010; Laurent et al. 2014; Mikkola et al. 2014; Joshi et al. 2017), many studies have revealed coeval emplacement of TTGs and sanukitoids in some Archean terranes (e.g., Limpopo Complex: Rajesh et al. 2018; São Francisco Craton: Bruno et al. 2020; parts of North China Craton: Jiang et al. 2016; Wang et al. 2024; and the Aravalli–BGC: Kaur et al. 2023a; this study).

There is a debate regarding the geodynamic environment for the emplacement of TTGs, such as (1) the melting of a continuously subducting oceanic slab or subducted oceanic plateaux (e.g. Drummond and Defant 1990; Moyen et al. 2003; Laurie et al. 2013; Martin et al. 2014; Palin et al. 2016; Hastie and Fitton 2019; Roman and Arndt 2020), and (2) melting within tectonically thickened mafic island–arc crust or at the base of a thick basaltic crust (Condie 2005; Bédard 2006, 2018; Huang et al. 2012; Nagel et al. 2012; Bédard et al. 2013; Johnson et al. 2017, 2019). The Jaisamand granitoids correspond to either high-HREE-Y or medium-HREE-Y groups (Fig. 9c), which were generated at shallow and relatively deep depths (> 30 km), respectively (Halla et al. 2009; Moyen 2011). The melting of crust at deeper levels in the Archean required the metabasites to be introduced deep into the mantle, as the weak Archean crust could not maintain a thickness of over 30 km due to the high heat flux from the mantle (Laurent et al. 2014 and references therein). The basaltic crust can be introduced into the deep mantle in a subduction setting. Furthermore, the Jaisamand sanukitoids (coeval with the TTGs) were generated by the transformation of TTG melts after interacting to varying degrees with the overlying mantle peridotite. This implies the coeval melting of basaltic crust and the overlying mantle peridotite for the formation of the sanukitoids. Additionally, the generation of Jaisamand transitional TTGs requires the interaction of TTG melts with older local felsic continental crust. This scenario is possible if all the three lithologies (metabasite, mantle peridotite, and continental crust) are geometrically associated, fitting well in a subduction setting (cf. Laurent et al. 2014). Importantly, this setting can explain the coexistence of high-HREE-Y and medium-HREE-Y TTGs and sanukitoids.

A subduction-related setting for the Jaisamand granitoids is also supported by the biotite chemical data, indicating a calc-alkaline affinity (Fig. 5c), and the whole-rock geochemical data, showing alkali-calcic to calc-alkalic and magnesian affinities (Fig. 8c, d; Abdel-Rahman 1994; Frost et al. 2001). This interpretation is consistent with the decoupling between LILE and HFSE (Fig. 9b, d, f), that is, the high LILE/HFSE ratios, which are typical of magmas formed in subduction environments. Moreover, in the tectonic discrimination diagrams of Pearce et al. (1984), the Jaisamand granitoids (i.e., TTGs, sanukitoids, and transitional TTGs) indicate emplacement in a subduction-related setting (Fig. 13a, b). Additionally, the granitoids exhibit Nb/Nb* and Pb/Pb* ratios lower and higher than unity, respectively (Fig. 13c), further supporting a subduction-related origin (Sotiriou et al. 2023 and references therein).

Given this, a thermal anomaly is required to explain the simultaneous melting at shallow and deeper depths during the Neoarchean, as Earth's heat production progressively declined, leading not only to a decreased degree of slab melting but also shifting the melting to greater depths (Martin et al. 2009). The melting of basaltic crust at greater depths might have resulted in the formation of medium-HREE-Y TTGs and sanukitoids. In this context, it is pertinent to note that the Archean subducting slab was not stable and was subjected to frequent slab break-offs (van Hunen and Moyen 2012). Therefore, the simultaneous low-P and high-P melting may have been achieved by slab break-off, consistent with the instability of subducting slab during the Neoarchean. Slab break-off led to the upwelling of hot asthenosphere, which further triggered the partial melting of the subducting slab at shallow depths, the overlying mantle wedge, and the older TTG continental crust to form coeval Jaisamand high-HREE-Y TTG, sanukitoids, and the transitional TTGs, respectively (Fig. 14).

6 Conclusions

1. The Jaisamand granitoids, exposed in the southern Aravalli–BGC in northwest India, consist of nearly coeval Neoarchean sanukitoids, TTGs, and transitional TTGs. They are mostly magnesian, weakly to strongly peraluminous, and alkali-calcic to calc-alkalic in nature.
2. The Jaisamand TTGs were generated by the slab melting of metabasites at shallow to moderate depths (1.0–1.2 GPa), above the garnet-in line but still within the plagioclase stability field forming high-HREE-Y TTGs and medium-HREE-Y TTGs, respectively. The differential

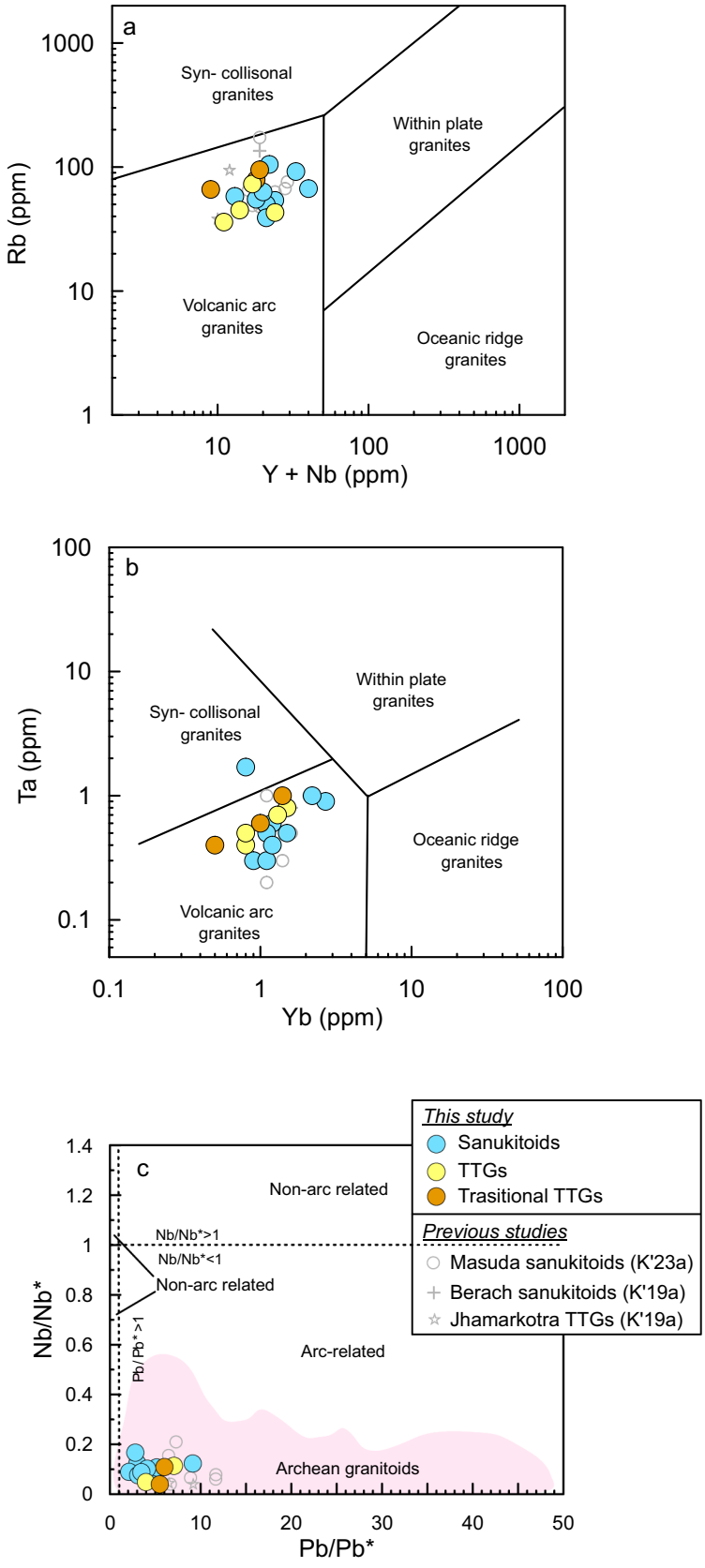

Fig. 13 Tectonic discrimination of the Jaisamand granitoids in: **a** Y + Nb (ppm) versus Rb (ppm) plot (Pearce et al. 1984); **b** Yb (ppm) versus Ta (ppm) diagram (Pearce et al. 1984) and **c** Pb/Pb* versus Nb/Nb* plot along with fields of Archean granitoids (Sotiriou et al. 2023). Previous studied samples are the same as in Fig. 10

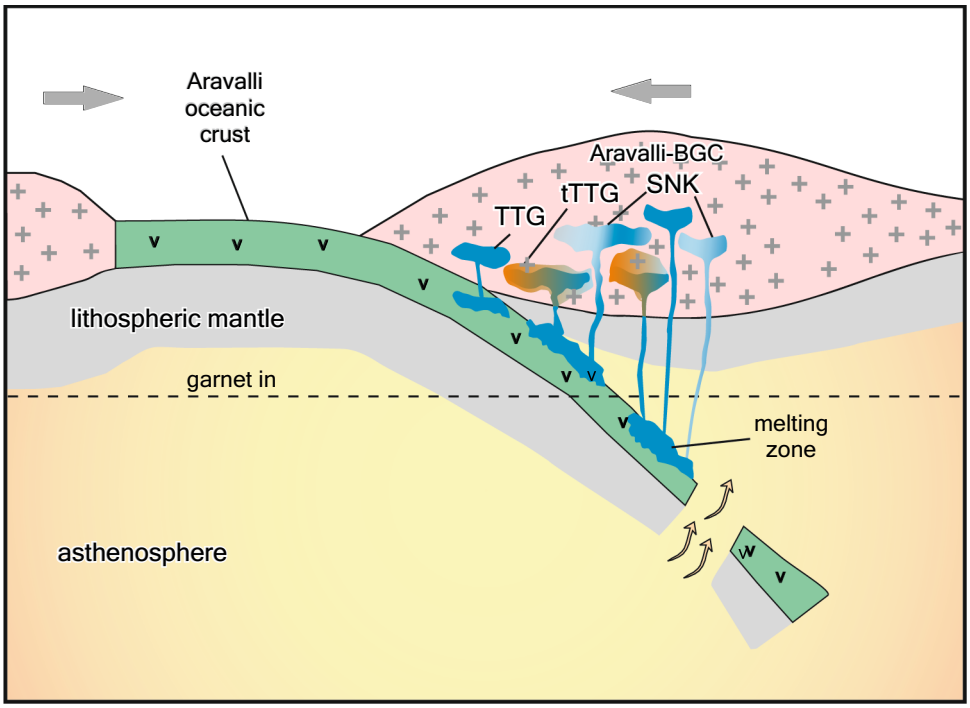

Fig. 14 Schematic geodynamic model showing the formation of Neoarchean Jaisamand TTGs, sanukitoids (*SNK*) and transitional TTGs (*tTTG*) in a subduction-related environment. See text for details

interaction of the ascending TTG melts with the overlying mantle wedge peridotite resulted in the formation of sanukitoids, while interactions between these TTGs melts and older TTGs at lower and middle crustal levels led to the formation of transitional TTGs.

3. The coexistence of high-HREE-Y and medium-HREE-Y TTGs and sanukitoids, coupled with high LILE/HFSE ratios, suggests a subduction-related setting for the Jaisamand granitoids.
4. Combined mineral chemical and whole-rock geochemical data, along with petrographic results, reveal albitization and silicification in some of the Jaisamand granitoids. These altered granitoids highlight the importance of determining plagioclase compositions, as failure to do so could lead to misleading characterization.

Acknowledgements We extend our gratitude to two anonymous reviewers for their critical comments that improved the manuscript immensely. We also thank Chiranjeeb Chatterjee for assistance during the EPMA work and to Rajiv Kumar for preparing the thin sections carefully.

Author contributions PD: methodology, formal analysis, investigation, writing—original draft; PK: conceptualization, investigation, formal analysis, writing—original draft, review and editing, supervision, funding acquisition; NC: conceptualization, investigation, writing—original draft, review and editing, supervision; SS: methodology, investigation.

Funding We also gratefully acknowledge the financial support provided by the Ministry of Earth Sciences, New Delhi (MoES/P.O/(Geo)/100(2)/2017).

Data availability All the data related to this work are available within as well as in the supplementary material of this article.

Declarations

Conflict of interest The authors declare that they have no conflict of interest.

References

Abdel-Rahman AM (1994) Nature of biotites from alkaline, calc-alkaline, and peraluminous magmas. J Petrol 35(2):525–541.

Acharyya SK (2003) The nature of Mesoproterozoic Central Indian tectonic zone with exhumed and reworked older granulites. Gondwana Res 6(2):197–214. https://doi.org/10.1016/S1342-937X(05)70970-9

Almeida JAC, Dall'Agnol R, Dias SB, Althoff FJ (2010) Origin of the Archean leucogranodiorite–granite suites: evidence from the Rio Maria terrane and implications for granite magmatism in the Archean. Lithos 120(3–4):235–257. https://doi.org/10.1016/j.lithos.2010.07.026

Almeida JAC, Dall'Agnol R, da Silva Leite AA (2013) Geochemistry and zircon geochronology of the Archean granite suites of the Rio Maria granite-greenstone terrane, Carajás Province, Brazil. J South Am Earth Sci 42:103–126. https://doi.org/10.1016/j.jsames.2012.10.008

Barker F (1979) Trondhjemite: definition, environment and hypotheses of origin. In: Barker F (ed) Developments in petrology.

Elsevier, Amsterdam, pp 1–12. https://doi.org/10.1016/b978-0-444-41765-7.50006-x
Barker F, Arth JG (1976) Generation of trondhjemitic-tonalitic liquids and Archean bimodal trondhjemite-basalt suites. Geology 4(10):596–600. https://doi.org/10.1130/0091-7613(1976)4%3c596:GOTLAA%3e2.0.CO;2
Barrat JA, Zanda B, Moynier F, Bollinger C, Liorzou C, Bayon G (2012) Geochemistry of CI chondrites: major and trace elements, and Cu and Zn isotopes. Geochim Cosmochim Acta 83:79–92. https://doi.org/10.1016/j.gca.2011.12.011
Bédard JH (2006) A catalytic delamination-driven model for coupled genesis of Archaean crust and sub-continental lithospheric mantle. Geochim Cosmochim Acta 70(5):1188–1214. https://doi.org/10.1016/j.gca.2005.11.008
Bédard JH (2018) Stagnant lids and mantle overturns: implications for Archaean tectonics, magmagenesis, crustal growth, mantle evolution, and the start of plate tectonics. Geosci Front 9(1):19–49. https://doi.org/10.1016/j.gsf.2017.01.005
Bédard JH, Harris LB, Thurston PC (2013) The hunting of the SnArc. Precambrian Res 229:20–48. https://doi.org/10.1016/j.precamres.2012.04.001
Boulvais P, Ruffet G, Cornichet J, Mermet M (2007) Cretaceous albitization and dequartzification of Hercynian peraluminous granite in the Salvezines Massif (French Pyrénées). Lithos 93(1–2):89–106. https://doi.org/10.1016/j.lithos.2006.05.001
Bowring SA, Williams IS (1999) Priscoan (4.00–4.03 Ga) orthogneisses from northwestern Canada. Contrib Mineral Petrol 134(1):3–16. https://doi.org/10.1007/s004100050465
Bruno H, Elizeu V, Heilbron M, Valeriano CM, Strachan R, Fowler M, Bersan S, Moreira H, Dussin I, Silva LGE, Tupinambá M, Almeida J, Neto C, Storey C (2020) Neoarchean and Rhyacian TTG-sanukitoid suites in the southern São Francisco Paleocontinent, Brazil: evidence for diachronous change towards modern tectonics. Geosci Front 11(5):1763–1787. https://doi.org/10.1016/j.gsf.2020.01.015
Bucholz CE, Spencer CJ (2019) Strongly peraluminous granites across the Archean-Proterozoic transition. J Petrol 60(7):1299–1348. https://doi.org/10.1093/petrology/egz033
Champion DC, Smithies RH (2001) Archaean granites of the Yilgarn and Pilbara cratons, Western Australia. In: Cassidy KF, Dunphy JM, Van Kranendonk MJ (eds) Proceedings of the Fourth International Archaean Symposium. AGSO Geosci Aus., Perth, Australia, pp 134–136 (Record 2001/37).
Champion DC, Smithies RH (2003) Archaean granites. In: Blevin PL, Chappell, BW, Jones M (eds) Magmas to mineralisation: the Ishihara symposium. AGSO Geosci Aus, pp 19–24 (Record 2003/14).
Champion DC, Smithies RH (2007) Geochemistry of Paleoarchean granites of the East Pilbara Terrane, Pilbara craton, Western Australia: Implications for Early Archean crustal growth. In: Van Kranendonk MJ, Bennett VC, Hoffmann JE (eds) Earth's oldest rocks. Developments in Precambrian geology, vol 15. Elsevier, Amsterdam, pp 369–409.
Champion DC, Smithies RH (2019) Geochemistry of Paleoarchean granites of the Eastern Pilbara Terrane, Pilbara Craton, Western Australia: implications for Early Archean crustal growth. In: Van Kranendonk MJ, Bennett VC, Hoffmann JE (eds) Earth's oldest rocks, 2nd edn. Elsevier, pp 487–517
Condie KC (2005) TTGs and adakites: Are they both slab melts? Lithos 80(1–4):33–44. https://doi.org/10.1016/j.lithos.2003.11.001
Condie KC (2018) A planet in transition: the onset of plate tectonics on Earth between 3 and 2 Ga? Geosci Front 9(1):51–60. https://doi.org/10.1016/j.gsf.2016.09.001
Condie KC, Belousova E, Griffin WL, Sircombe KN (2009) Granitoid events in space and time: Constraints from igneous and detrital zircon age spectra. Gondwana Res 15(3–4):228–242. https://doi.org/10.1016/j.gr.2008.06.001
Condie KC (1981) Archaean greenstone belts. In: Developments in Precambrian geology. Elsevier, pp 434.
Crawford ML, Hollister LS (1982) Contrast of metamorphic and structural histories across the work channel lineament, Coast Plutonic Complex, British Columbia. J Geophys Res 87(B5):3849–3860. https://doi.org/10.1029/jb087ib05p03849
Deer WA, Howie RA, Zussman J (2013) An introduction to the rock-forming minerals. In: Mineralogical Society of Great Britain and Ireland, 3rd ed, pp 498.
Dhuime B, Wuestefeld A, Hawkesworth CJ (2015) Emergence of modern continental crust about 3 billion years ago. Nat Geosci 8:552–555. https://doi.org/10.1038/ngeo2466
Drummond MS, Defant MJ (1990) A model for trondhjemite-tonalite-dacite genesis and crustal growth via slab melting—Archean to modern comparisons. J Geophys Res 95(B13):21503–21521. https://doi.org/10.1029/JB095iB13p21503
Engvik AK, Putnis A, Fitz Gerald JD, Austrheim H (2008) Albitization of granitic rocks: the mechanism of replacement of oligoclase by albite. Can Mineral 46(6):1401–1415. https://doi.org/10.3749/canmin.46.6.1401
Eriksson PG, Mazumder R, Sarkar S, Bose PK, Altermann W, van der Merwe R (1999) The 2.7–2.0 Ga volcano-sedimentary record of Africa, India and Australia: evidence for global and local changes in sea level and continental freeboard. Precambrian Res 97(3–4):269–302. https://doi.org/10.1016/S0301-9268(99)00035-2
Evans BW, Vance JA (1987) Epidote phenocrysts in dacitic dikes, Boulder County, Colorado. Contrib Mineral Petrol 96(2):178–185. https://doi.org/10.1007/BF00375231
Foley S, Tiepolo M, Vannucci R (2002) Growth of early continental crust controlled by melting of amphibolite in subduction zones. Nature 417(6891):837–840. https://doi.org/10.1038/nature00799
Frost BR, Frost CD (2008) A geochemical classification for feldspathic igneous rocks. J Petrol 49(11):1955–1969. https://doi.org/10.1093/petrology/egn054
Frost BR, Barnes CG, Collins WJ, Arculus RJ, Ellis DJ, Frost CD (2001) A geochemical classification for granitic rocks. J Petrol 42(11):2033–2048. https://doi.org/10.1093/petrology/42.11.2033
Glikson AY (1979) Early Precambrian tonalite-trondhjemite sialic nuclei. Earth-Sci Rev 15(1):1–73. https://doi.org/10.1016/0012-8252(79)90043-6
Gopalan K, MacDougall JD, Roy AB, Murali AV (1990) Sm-Nd evidence for 3.3 Ga old rocks in Rajasthan, northwestern India. Precambrian Res 48(3):287–297. https://doi.org/10.1016/0301-9268(90)90013-G
Gupta SN, Arora YK, Mathur RK, Iqbaluddin, Prasad B, Sahai TN, Sharma SB (1997) The Precambrian geology of the Aravalli region, southern Rajasthan and northeastern Gujarat. Mem Geol Surv India 123:262
Hahn G, Kodl G, de Wall H, Schulz B, Bestmann M, Chauhan NK (2020) Deformation in the Aravalli Supergroup, Aravalli-Delhi Mobile Belt, NW India and tectonic significance. In: Biswal T, Ray S, Grasemann B (eds) Structural geometry of mobile belts of the Indian Subcontinent. Society of Earth Scientists Series. Springer, Cham, pp 23–55. https://doi.org/10.1007/978-3-030-40593-9_2
Halla J (2005) Late Archean high-Mg granitoids (sanukitoids) in the southern Karelian domain, eastern Finland: Pb and Nd isotopic constraints on crust — mantle interactions. Lithos 79(1–2):161–178. https://doi.org/10.1016/j.lithos.2004.05.007
Halla J, van Hunen J, Heilimo E, Hölttä P (2009) Geochemical and numerical constraints on Neoarchean plate tectonics. Precambrian Res 174(1–2):155–162. https://doi.org/10.1016/j.precamres.2009.07.008

Hastie AR, Fitton JG (2019) Eoarchaean tectonics: new constraints from high pressure-temperature experiments and mass balance modelling. Precambrian Res 325:20–38. https://doi.org/10.1016/j.precamres.2019.02.006

Hawkesworth CJ, Dhuime B, Pietranik AB, Cawood PA, Kemp AIS, Storey CD (2010) The generation and evolution of the continental crust. J Geol Soc 167(2):229–248. https://doi.org/10.1144/0016-76492009-072

Heilimo E, Halla J, Hölttä P (2010) Discrimination and origin of the sanukitoid series: geochemical constraints from the Neoarchean western Karelian Province (Finland). Lithos 115(1–4):27–39. https://doi.org/10.1016/j.lithos.2009.11.001

Heilimo E, Halla J, Huhma H (2011) Single-grain zircon U-Pb age constraints of the western and eastern sanukitoid zones in the Finnish part of the Karelian Province. Lithos 121(1–4):87–99. https://doi.org/10.1016/j.lithos.2010.10.006

Heron AM (1953) The geology of central Rajputana. Mem Geol Surv India 79:389.

Hu Y, Liu S, Gao L, Sun G, Guo R, Fu J, Wang M, Hu F (2019) Diverse middle Neoarchean granitoids and the delamination of thickened crust in the Western Shandong Terrane, North China Craton. Lithos 348:105178. https://doi.org/10.1016/j.lithos.2019.105178

Huang H, Polat A, Fryer BJ, Appel PWU, Windley BF (2012) Geochemistry of the Mesoarchean Fiskenæsset complex at Majorqap qâva, SW Greenland: evidence for two different magma compositions. Chem Geol 314 – 317:66–82. https://doi.org/10.1016/j.chemgeo.2012.04.020

Iizuka T, Horie K, Komiya T, Maruyama S, Hirata T, Hidaka H, Windley BF (2006) 4.2 Ga zircon xenocryst in an Acasta gneiss from northwestern Canada: evidence for early continental crust. Geology 34(4):245 – 248. https://doi.org/10.1130/g22124.1

Jahn BM, Glikson AY, Peucat JJ, Hickman AH (1981) REE geochemistry and isotopic data of Archean silicic volcanics and granitoids from the Pilbara block, western Australia: implications for the early crustal evolution. Geochim Cosmochim Acta 45(9):1633–1652. https://doi.org/10.1016/S0016-7037(81)80002-6

Jain SC, Yedekar DB, Nair KKK (1991) Central Indian shear zone: A major Precambrian crustal boundary. J Geol Soc India 37:521–532.

Jayananda M, Aadhiseshan KR, Kusiak MA, Wilde SA, Sekhamo KU, Guitreau M, Santosh M, Gireesh RV (2020) Multi-stage crustal growth and Neoarchean geodynamics in the Eastern Dharwar Craton, southern India. Gondwana Res 78:228–260. https://doi.org/10.1016/j.gr.2019.09.005

Jiang N, Guo J, Fan W, Hu J, Zong K, Zhang S (2016) Archean TTGs and sanukitoids from the Jiaobei terrain, North China Craton: insights into crustal growth and mantle metasomatism. Precambrian Res 281:656–672. https://doi.org/10.1016/j.precamres.2016.06.019

Johnson TE, Brown M, Gardiner NJ, Kirkland CL, Smithies RH (2017) Earth's first stable continents did not form by subduction. Nature 543:239–242. https://doi.org/10.1038/nature21383

Johnson TE, Kirkland CL, Gardiner NJ, Brown M, Smithies RH, Santosh M (2019) Secular change in TTG compositions: implications for the evolution of Archaean geodynamics. Earth Planet Sci Lett 505:65–75. https://doi.org/10.1016/j.epsl.2018.10.022

Joshi BK, Bhattacharjee J, Rai G, Halla J, Ahmad T, Kurhila M, Heilimo E, Choudhary AK (2017) The diversification of granitoids and plate tectonic implications at the Archaean—Proterozoic boundary in the Bundelkhand Carton, Central India. In: Halla J, Whitehouse MJ, Ahmad T, Bagai Z (eds) Crust — mantle interactions and granitoid diversification: insights from Archaean Cratons, vol 449. Geological Society, London, Special Publications, London, pp 123–157

Kamber BS, Tomlinson EL (2019) Petrological, mineralogical and geochemical peculiarities of Archaean cratons. Chem Geol 511:123–151. https://doi.org/10.1016/j.chemgeo.2019.02.011

Kaur P, Zeh A, Chaudhri N, Gerdes A, Okrusch M (2011) Archaean to Palaeoproterozoic crustal evolution of the Aravalli mountain range, NW India, and its hinterland: the U-Pb and Hf isotope record of detrital zircon. Precambrian Res 187(1–2):155–164. https://doi.org/10.1016/j.precamres.2011.03.005

Kaur P, Chaudhri N, Hofmann AW, Raczek I, Okrusch M, Skora S, Baumgartner LP (2012) Two-stage, extreme albitization of A-type granites from Rajasthan, NW India. J Petrol 53(5):919–948. https://doi.org/10.1093/petrology/egs003

Kaur P, Zeh A, Chaudhri N, Gerdes A, Okrusch M (2013) Nature of magmatism and sedimentation at a Columbia active margin: insights from combined U-Pb and Lu–Hf isotope data of detrital zircons from NW India. Gondwana Res 23(3):1040–1052. https://doi.org/10.1016/j.gr.2012.07.008

Kaur P, Chaudhri N, Hofmann AW, Raczek I, Okrusch M, Skora S, Koepke J (2014) Metasomatism of ferroan granites in the northern Aravalli orogen, NW India: geochemical and isotopic constraints, and its metallogenic significance. Int J Earth Sci 103(4):1083–1112. https://doi.org/10.1007/s00531-014-1005-x

Kaur P, Chaudhri N, Hofmann AW (2015) New evidence for two sharp replacement fronts during albitization of granitoids from northern Aravalli orogen, northwest India. Int Geol Rev 57(11–12):1660–1685. https://doi.org/10.1080/00206814.2014.1000394

Kaur P, Zeh A, Chaudhri N (2017) Palaeoproterozoic continental arc magmatism, and Neoproterozoic metamorphism in the Aravalli-Delhi orogenic belt, NW India: new constraints from *in situ* zircon U-Pb-Hf isotope systematics, monazite dating and whole-rock geochemistry. J Asian Earth Sci 136:68–88. https://doi.org/10.1016/j.jseaes.2017.01.024

Kaur P, Zeh A, Chaudhri N (2019a) Archean crustal evolution of the Aravalli Banded Gneissic Complex, NW India: constraints from zircon U-Pb ages, Lu-Hf isotope systematics, and whole-rock geochemistry of granitoids. Precambrian Res 327:81–102. https://doi.org/10.1016/j.precamres.2019.03.004

Kaur P, Chaudhri N, Eliyas N (2019b) Origin of trondhjemite and albitite at the expense of A-type granite, Aravalli orogen, India: evidence from new metasomatic replacement fronts. Geosci Front 10(5):1891–1913. https://doi.org/10.1016/j.gsf.2018.09.019

Kaur P, Zeh A, Chaudhri N (2021) Archean to Proterozoic (3535–900 Ma) crustal evolution of the central Aravalli Banded Gneissic Complex, NW India: new constraints from zircon U-Pb-Hf isotopes and geochemistry. Precambrian Res 359:106179. https://doi.org/10.1016/j.precamres.2021.106179

Kaur P, Zeh A, Chaudhri N, Dutta P (2022) Detrital zircon U-Pb-Hf isotope record of conglomerates in the southern Aravalli orogen, NW India: implications for stratigraphy, provenance and Archean to Paleoproterozoic crustal evolution. Precambrian Res 379:106800. https://doi.org/10.1016/j.precamres.2022.106800

Kaur P, Zeh A, Chaudhri N, Sharma S (2023a) Neoarchean to Paleoproterozoic crustal evolution of the central Aravalli-Banded Gneissic Complex (NW India): evidence from zircon U-Pb-Hf isotope systematics and whole-rock composition of Neoarchean sanukitoids, Paleoproterozoic granitoids and metasedimentary rocks. Precambrian Res 399:107236. https://doi.org/10.1016/j.precamres.2023.107236

Kaur P, Zeh A, Chaudhri N, Manisha, Tiwana JK, Dutta P (2023b) Stenian sediments (<1065 Ma) and Tonian A- and I-type magmatism (1000–970 Ma) along the western margin of the central Aravalli orogen, NW India: petrogenetic and geodynamic implications. Gondwana Res 117:23–40. https://doi.org/10.1016/j.gr.2023.01.006

Kaur P, Chaudhri N, Saha L, Nasipuri P (2024a) Crustal evolution of the Aravalli and Bundelkhand Archean nuclei, North

Indian Block: recent advances and perspectives. Proc Indian Natl Sci Acad 90(2):196–208. https://doi.org/10.1007/s43538-024-00278-x

Kaur P, Manisha, Dutta P, Sharma S, Chaudhri N (2024b) Geochemical constraints on the provenance and tectonic setting of metasedimentary rocks from the South Delhi Supergroup, NW India: implications for tectonic evolution of western margin of the Aravalli orogen. Int Geol Rev 66(6):1280–1301. https://doi.org/10.1080/00206814.2023.2233024

Kemp AIS, Wilde SA, Hawkesworth CJ, Coath CD, Nemchin A, Pidgeon RT, Vervoort JD, DuFrane SA (2010) Hadean crustal evolution revisited: new constraints from Pb–Hf isotope systematics of the Jack Hills zircons. Earth Planet Sci Lett 296(1–2):45–56. https://doi.org/10.1016/j.epsl.2010.04.043

Kendrick J, Duguet M, Kirkland CL, Liebmann J, Moser DE, Vervoort JD, Yakymchuk C (2024) Testing the TTG–metabasite connection in the southern Superior Province: an integrated geochemical, isotopic, and petrogenetic modelling approach. J Petrol 65(7):egae066. https://doi.org/10.1093/petrology/egae066

Laurent O, Martin H, Doucelance R, Moyen JF, Paquette JL (2011) Geochemistry and petrogenesis of high-K "sanukitoids" from the Bulai pluton, Central Limpopo Belt, South Africa: implications for geodynamic changes at the Archaean-Proterozoic boundary. Lithos 123(1–4):73–91. https://doi.org/10.1016/j.lithos.2010.12.009

Laurent O, Doucelance R, Martin H, Moyen JF (2013) Differentiation of the late-Archaean sanukitoid series and some implications for crustal growth: insights from geochemical modelling on the Bulai pluton, Central Limpopo Belt, South Africa. Precambrian Res 227:186–203. https://doi.org/10.1016/j.precamres.2012.07.004

Laurent O, Martin H, Moyen JF, Doucelance R (2014) The diversity and evolution of late-Archean granitoids: evidence for the onset of "modern-style" plate tectonics between 3.0 and 2.5 Ga. Lithos 205:208–235. https://doi.org/10.1016/j.lithos.2014.06.012

Laurent O, Guitreau M, Bruand E, Moyen JF (2024) At the dawn of continents: Archean tonalite-trondhjemite-granodiorite suites. Elements 20(3):174–179. https://doi.org/10.2138/gselements.20.3.174

Laurie A, Stevens G, van Hunen J (2013) The end of continental growth by TTG magmatism. Terra Nova 25(2):130–136. https://doi.org/10.1111/ter.12015

Liou JG (1973) Synthesis and stability relations of epidote, $Ca_2Al_2FeSi_3O_{12}$ (OH). J Petrol 14(3):381–413. https://doi.org/10.1093/petrology/14.3.381

López S, Fernández C, Castro A (2006) Evolution of the Archean continental crust: Insights from the experimental study of Archean granitoids. Curr Sci 91:607–621.

Maniar PD, Piccoli PM (1989) Tectonic discrimination of granitoids. Geol Soc Am Bull 101(5):635–643. https://doi.org/10.1130/0016-7606(1989)101%3c0635:TDOG%3e2.3.CO;2

Martin H (1986) Effect of steeper Archean geothermal gradient on geochemistry of subduction-zone magmas. Geology 14(9):753. https://doi.org/10.1130/0091-7613(1986)14%3c753:eosagg%3e2.0.co;2

Martin H (1993) The mechanisms of petrogenesis of the Archaean continental crust: comparison with modern processes. Lithos 30(3–4):373–388. https://doi.org/10.1016/0024-4937(93)90046-F

Martin H, Moyen JF (2002) Secular changes in tonalite-trondhjemite-granodiorite composition as markers of the progressive cooling of Earth. Geology 30(4):319–322. https://doi.org/10.1130/0091-7613(2002)030%3C0319:SCITTG%3E2.0.CO;2

Martin H, Smithies RH, Rapp R, Moyen JF, Champion D (2005) An overview of adakite, tonalite–trondhjemite–granodiorite (TTG), and sanukitoid: relationships and some implications for crustal evolution. Lithos 79(1–2):1–24. https://doi.org/10.1016/j.lithos.2004.04.048

Martin H, Moyen JF, Rapp R (2009) The sanukitoid series: magmatism at the Archaean-Proterozoic transition. Earth Environ Sci Trans R Soc Edinb 100(1–2):15–33. https://doi.org/10.1017/s1755691009016120

Martin H, Moyen JF, Guitreau M, Blichert-Toft J, Le Pennec JL (2014) Why Archaean TTG cannot be generated by MORB melting in subduction zones. Lithos 198–199:1–13. https://doi.org/10.1016/j.lithos.2014.02.017

McDonough W, Sun SS (1995) The composition of the Earth. Chem Geol 120 (3–4):223–253. https://doi.org/10.1016/0009-2541(94)00140-4

McKenzie NR, Hughes NC, Myrow PM, Banerjee DM, Deb M, Planavsky NJ (2013) New age constraints for the Proterozoic Aravalli-Delhi successions of India and their implications. Precambrian Res 238:120–128. https://doi.org/10.1016/j.precamres.2013.10.006

Mikkola P, Heilimo E, Huhma H (2014) Relationships between sanukitoids and crust-derived melts and their implications for the diversity of Neoarchaean granitoids: a case study from Surmansuo and nearby areas, eastern Finland. Bull Geol Soc Finl 86(1):23–40. https://doi.org/10.17741/bgsf/86.1.002

Mondal MEA, Raza A (2013) Geochemistry of sanukitoid series granitoids from the Neoarchaean Berach granitoid batholith, Aravalli craton, northwestern Indian shield. Curr Sci 105:102–108.

Moore DE, Liou JG (1979) Chessboard-twinned albite from Franciscan meta-conglomerates of the Diablo range, California. Am Mineral 64(3–4):329–336.

Moyen JF (2011) The composite Archaean grey gneisses: petrological significance, and evidence for a non-unique tectonic setting for Archaean crustal growth. Lithos 123(1–4):21–36. https://doi.org/10.1016/j.lithos.2010.09.015

Moyen JF, Laurent O (2018) Archaean tectonic systems: a view from igneous rocks. Lithos 302:99–125. https://doi.org/10.1016/j.lithos.2017.11.038

Moyen JF, Martin H (2012) Forty years of TTG research. Lithos 148:312–336. https://doi.org/10.1016/J.LITHOS.2012.06.010

Moyen JF, Martin H, Jayananda M (2001) Multi-element geochemical modelling of crust–mantle interactions during late-Archaean crustal growth: the Closepet granite (South India). Precambrian Res 112(1–2):87–105. https://doi.org/10.1016/S0301-9268(01)00171-1

Moyen JF, Martin H, Jayananda M, Auvray B (2003) Late Archaean granites: a typology based on the Dharwar Craton (India). Precambrian Res 127(1–3):103–123. https://doi.org/10.1016/S0301-9268(03)00183-9

Nagel TJ, Hoffmann JE, Münker C (2012) Generation of Eoarchean tonalite-trondhjemite-granodiorite series from thickened mafic arc crust. Geology 40(4):375–378. https://doi.org/10.1130/G32729.1

Naney MT (1983) Phase equilibria of rock-forming ferromagnesian silicates in granitic systems. Am J Sci 283(10):993–1033. https://doi.org/10.2475/ajs.283.10.993

Naqvi SM, Rogers JJW (1987) Precambrian geology of India. Oxford University Press, New York.

Narduzzi F, Farina F, Stevens G, Lana C, Nalini Jr HA (2017) Magmatic garnet in the Cordilleran-type Galiléia granitoids of the Araçuaí belt (Brazil): evidence for crystallization in the lower crust. Lithos 282:82–97. https://doi.org/10.1016/j.lithos.2017.02.017

Nutman AP (2006) Antiquity of the oceans and continents. Elements 2(4):223–227. https://doi.org/10.2113/gselements.2.4.223

Oliveira MA, Dall'Agnol R, Almeida JAC (2011) Petrology of the Mesoarchean Rio Maria suite and the discrimination of sanukitoid

series. Lithos 127(1–2):192–209. https://doi.org/10.1016/j.lithos.2011.08.017
Orville PM (1963) Alkali ion exchange between vapor and feldspar phases. Am J Sci 261(3):201–237. https://doi.org/10.2475/ajs.261.3.201
Palin RM, White RW, Green ECR (2016) Partial melting of metabasic rocks and the generation of tonalitic–trondhjemitic–granodioritic (TTG) crust in the Archaean: constraints from phase equilibrium modelling. Precambrian Res 287:73–90. https://doi.org/10.1016/j.precamres.2016.11.001
Palme H, O'Neill H (2014) Cosmochemical estimates of mantle composition. In: Holland HD, Turekian KK (eds) Treatise on geochemistry. Elsevier, Amsterdam, pp 1–39. https://doi.org/10.1016/b978-0-08-095975-7.00201-1
Patiño Douce AE (1999) What do experiments tell us about the relative contributions of crust and mantle to the origin of granitic magmas? Geol Soc Lond Spec Publ 168(1):55–75. https://doi.org/10.1144/GSL.SP.1999.168.01.05
Pearce JA, Harris NBW, Tindle AG (1984) Trace element discrimination diagrams for the tectonic interpretation of granitic rocks. J Petrol 25(4):956–983. https://doi.org/10.1093/petrology/25.4.956
Plümper O, Putnis A (2009) The complex hydrothermal history of granitic rocks: multiple feldspar replacement reactions under subsolidus conditions. J Petrol 50(5):967–987. https://doi.org/10.1093/petrology/egp028
Prouteau G, Scaillet B, Pichavant M, Maury R (2001) Evidence for mantle metasomatism by hydrous silicic melts derived from subducted oceanic crust. Nature 410(6825):197–200. https://doi.org/10.1038/35065583
Qian Q, Hermann J (2013) Partial melting of lower crust at 10–15kbar: constraints on adakite and TTG formation. Contrib Mineral Petrol 165(6):1195–1224. https://doi.org/10.1007/s00410-013-0854-9
Rahaman MS, Mondal MEA (2015) Evolution of continental crust of the Aravalli craton, NW India, during the Neoarchaean–Palaeoproterozoic: evidence from geochemistry of granitoids. Int Geol Rev 57(11–12):1510–1525. https://doi.org/10.1080/00206814.2014.950607
Rajesh HM, Belyanin GA, Van Reenen DD (2018) Three tier transition of Neoarchean TTG-sanukitoid magmatism in the Beit Bridge Complex, southern Africa. Lithos 296:431–451. https://doi.org/10.1016/j.lithos.2017.11.018
Rapp RP, Watson EB, Miller CF (1991) Partial melting of amphibolite/eclogite and the origin of Archean trondhjemites and tonalites. Precambrian Res 51(1–4):1–25. https://doi.org/10.1016/0301-9268(91)90092-O
Rapp RP, Shimizu N, Norman MD, Applegate GS (1999) Reaction between slab-derived melts and peridotite in the mantle wedge: experimental constraints at 3.8 GPa. Chem Geol 160(4):335–356. https://doi.org/10.1016/S0009-2541(99)00106-0
Rapp RP, Shimizu N, Norman MD (2003) Growth of early continental crust by partial melting of eclogite. Nature 425(6958):605–609. https://doi.org/10.1038/nature02031
Rapp RP, Norman MD, Laporte D, Yaxley GM, Martin H, Foley SF (2010) Continent formation in the Archean and chemical evolution of the cratonic lithosphere: melt–rock reaction experiments at 3–4 GPa and petrogenesis of Archean Mg-diorites (Sanukitoids). J Petrol 51(6):1237–1266. https://doi.org/10.1093/petrology/egq017
Rickwood PC (1989) Boundary lines within petrologic diagrams which use oxides of major and minor elements. Lithos 22(4):247–263. https://doi.org/10.1016/0024-4937(89)90028-5
Rollinson H (2017) There were no large volumes of felsic continental crust in the early Earth. Geosphere 13(2):235–246. https://doi.org/10.1130/ges01437.1
Rollinson H, Chagondah G, Hofmann A (2024) The late archaean granite paradox: a case study from the Zimbabwe Craton. Precambrian Res 410:107491. https://doi.org/10.1016/j.precamres.2024.107491
Roman A, Arndt N (2020) Differentiated Archean oceanic crust: its thermal structure, mechanical stability and a test of the sagduction hypothesis. Geochim Cosmochim Acta 278:65–77. https://doi.org/10.1016/j.gca.2019.07.009
Roy AB (2012) Indian shield: Insight into the pristine size, shape and tectonic framework. Indian J Geosci 66:181–192.
Roy AB, Kröner A (1996) Single zircon evaporation ages constraining the growth of the Archaean Aravalli craton, northwestern Indian shield. Geol Mag 133(3):333–342. https://doi.org/10.1017/s0016756800009067
Roy AB, Jakhar SR (2002) Geology of Rajasthan (Northwest India) Precambrian to Recent. Scientific Publishers, Jodhpur, India, pp 421
Schiano P, Monzier M, Eissen JP, Martin H, Koga KT (2010) Simple mixing as the major control of the evolution of volcanic suites in the Ecuadorian Andes. Contrib Mineral Petrol 160(2):297–312. https://doi.org/10.1007/s00410-009-0478-2
Schmidt MW, Poli S (2004) Magmatic epidote. Rev Mineral Geochem 56(1):399–430. https://doi.org/10.2138/gsrmg.56.1.399
Schmidt MW, Thompson AB (1996) Epidote in calc-alkaline magmas: an experimental study of stability, phase relationships, and the role of epidote in magmatic evolution. Am Mineral 81(3–4):462–474. https://doi.org/10.2138/am-1996-3-420
Sharma RS (1988) Pattern of metamorphism in the Precambrian rocks of the Aravalli Mountain Belt. In: Roy AB (ed) Precambrian of the Aravalli Mountain, Rajasthan, vol 7. Memoirs of the Geological Survey of India, pp 33–75
Shekhawat LS, Joshi DW, Pandit MK (2001) A relook into the status of granitoids and conglomerate in Salumber—Jaisamand area, southern Rajasthan: implications for the stratigraphy of the Palaeoproterozoic Aravalli fold belt. J Geol Soc India 58:53–63
Shirey SB, Hanson GN (1984) Mantle-derived Archaean monzodiorites and trachyandesites. Nature 310:222–224. https://doi.org/10.1038/310222a0
Singh PK, Verma SK, Singh VK, Moreno JA, Oliveira EP, Li XH, Malviya VP, Prakash D (2021) Geochronology and petrogenesis of the TTG gneisses and granitoids from the central Bundelkhand granite-greenstone terrane, Bundelkhand Craton, India: implications for Archean crustal evolution and cratonization. Precambrian Res 359:106210. https://doi.org/10.1016/j.precamres.2021.106210
Siqueira R, Sial AN, Ferreira VP (2021) Crystallization conditions of two adjacent epidote + diopside-bearing granitic stocks, northeastern Brazil. An Acad Bras Cienc 93(suppl 4):e20210535. https://doi.org/10.1590/0001-3765202120210535
Sisson TW, Ratajeski K, Hankins WB, Glazner AF (2005) Voluminous granitic magmas from common basaltic sources. Contrib Mineral Petrol 148(6):635–661. https://doi.org/10.1007/s00410-004-0632-9
Smithies RH (2000) The Archaean tonalite–trondhjemite–granodiorite (TTG) series is not an analogue of Cenozoic adakite. Earth Planet Sci Lett 182(1):115–125. https://doi.org/10.1016/S0012-821X(00)00236-3
Smithies RH, Lu YJ, Johnson TE, Kirkland CL, Cassidy KF, Champion DC, Mole DR, Zibra I, Gessner K, Sapkota J, De Paoli MC, Poujol M (2019) No evidence for high-pressure melting of Earth's crust in the Archean. Nat Commun 10(1):5559. https://doi.org/10.1038/s41467-019-13547-x
Sotiriou P, Polat A, Windley B, Kusky T (2023) Temporal variations in the incompatible trace element systematics of Archean TTGs: implications for crustal growth and tectonic processes in the early Earth. Earth Sci Rev 236:104274. https://doi.org/10.1016/j.earscirev.2022.104274

Stern R, Bleeker W (1998) Age of the world's oldest rocks refined using Canada's SHRIMP: The Acasta Gneiss complex, Northwest Territories, Canada. Geosci Can 25:27–31.

Stern RA, Hanson GN (1991) Archean high-Mg granodiorite: a derivative of light rare earth element-enriched monzodiorite of mantle origin. J Petrol 32(1):201–238. https://doi.org/10.1093/petrology/32.1.201

Stern CR, Kilian R (1996) Role of the subducted slab, mantle wedge and continental crust in the generation of adakites from the Andean Austral Volcanic Zone. Contrib Mineral Petrol 123(3):263–281. https://doi.org/10.1007/s004100050155

Streckeisen A (1976) To each plutonic rock its proper name. Earth-Sci Rev 12(1):1–33. https://doi.org/10.1016/0012-8252(76)90052-0

Sun G, Liu S, Li S, Bao H, Wang W, Guo R, Fu J, Gao L, Hu Y, Wang X, Yu S, Dai L (2024) Neoarchean granitoid magmatism and geodynamic process in the northeastern North China Craton. Geol Soc Am Bull. https://doi.org/10.1130/B37584.1

Sylvester PJ (1994) Archean granite plutons. In: Developments in Precambrian geology. Elsevier, Amsterdam, pp 261–314. https://doi.org/10.1016/s0166-2635(08)70225-1

Tang M, Chen K, Rudnick RL (2016) Archean upper crust transition from mafic to felsic marks the onset of plate tectonics. Science 351(6271):372–375. https://doi.org/10.1126/science.aad5513

Tulloch AJ (1986) Comments and reply on "Implications of magmatic epidote-bearing plutons on crustal evolution in the accreted terranes of northwestern North America" and "Magmatic epidote and its petrologic significance." Geology 14(2):186–187. https://doi.org/10.1130/0091-7613(1986)14<186:caroio>2.0.co;2

van Hunen J, Moyen JF (2012) Archean subduction: fact or fiction? Annu Rev Earth Planet Sci 40:195–219. https://doi.org/10.1146/annurev-earth-042711-105255

Wan Y, Dong C, Liu D, Kröner A, Yang C, Wang W, Du L, Xie H, Ma M (2012) Zircon ages and geochemistry of late neoarchean syenogranites in the North China Craton: a review. Precambrian Res 222:265–289. https://doi.org/10.1016/j.precamres.2011.05.001

Wang Y, Zhang Y, Zhao G, Fan W, Xia X, Zhang F, Zhang A (2009) Zircon U-Pb geochronological and geochemical constraints on the petrogenesis of the Taishan sanukitoids (Shandong): implications for Neoarchean subduction in the eastern block, North China Craton. Precambrian Res 174(3–4):273–286. https://doi.org/10.1016/j.precamres.2009.08.005

Wang W, Cawood PA, Pandit MK, Zhou MF, Chen WT (2017) Zircon U-Pb age and Hf isotope evidence for an Eoarchaean crustal remnant and episodic crustal reworking in response to supercontinent cycles in NW India. J Geol Soc 174(4):759–772. https://doi.org/10.1144/jgs2016-080

Wang W, Cawood PA, Pandit MK, Zhou MF, Zhao JH (2019) Evolving passive- and active-margin tectonics of the Paleoproterozoic Aravalli Basin, NW India. Geol Soc Am Bull 131(3–4):426–443. https://doi.org/10.1130/B35027.1

Wang W, Lu Y, Gao L, Sun G, Zhou XZ Yao J, Yang W, Liang X (2024) Late Archean K-rich intermediate magmatism driven by deep supracrustal recycling. Chem Geol 662:122215. https://doi.org/10.1016/j.chemgeo.2024.122215

Whitney DL, Evans BW (2010) Abbreviations for names of rock-forming minerals. Am Mineral 95(1):185–187. https://doi.org/10.2138/am.2010.3371

Wiedenbeck M, Goswami JN (1994) High precision $^{207}Pb/^{206}Pb$ zircon geochronology using a small ion microprobe. Geochim Cosmochim Acta 58(9):2135–2141. https://doi.org/10.1016/0016-7037(94)90291-7

Wiedenbeck M, Goswami JN, Roy AB (1996) Stabilization of the Aravalli craton of northwestern India at 2.5 Ga: an ion microprobe zircon study. Chem Geol 129(3–4):325–340. https://doi.org/10.1016/0009-2541(95)00182-4

Windley BF, Kusky T, Polat A (2021) Onset of plate tectonics by the Eoarchean. Precambrian Res 352:105980. https://doi.org/10.1016/j.precamres.2020.105980

Wiszniewska J, Grabarczyk A, Krzemińska E, Ahmad T (2020) Contribution to the mineral chemistry of the Proterozoic Aravalli mafic meta-volcanic rocks from Rajasthan, NW India. Minerals 10(7):638. https://doi.org/10.3390/min10070638

Zane A, Weiss Z (1998) A procedure for classifying rock-forming chlorites based on microprobe data. Rend Fis Acc Lincei 9(1):51–56. https://doi.org/10.1007/BF02904455

Zen E-an (1988) Tectonic significance of high-pressure plutonic rocks in the western cordillera of North America. In: Ernst WG (ed) Metamorphism and crustal evolution of the western United States, Rube 7. Prentice-Hall, Englewood Cliffs, pp 41–67

Zen E-an, Hammarstrom JM (1984) Magmatic epidote and its petrologic significance. Geology 12(9):515 – 518. https://doi.org/10.1130/0091-7613(1984)12<515:MEAIPS>2.0.CO;2

Zhao XF, Zhou MF, Li JW, Wu FY (2008) Association of Neoproterozoic A- and I-type granites in South China: implications for generation of A-type granites in a subduction-related environment. Chem Geol 257(1–2):1–15. https://doi.org/10.1016/j.chemgeo.2008.07.018